Materials Science & Engineering A 814 (2021) 141237

Contents lists available at ScienceDirect

Materials Science & Engineering A

journal homepage: http://www.elsevier.com/locate/msea

Material modeling of Ti–6Al–4V alloy processed by laser powder bed fusion for application in macro-scale process simulation

Katharina Bartsch *, Dirk Herzog, Bastian Bossen, Claus Emmelmann

Hamburg University of Technology TUHH, Institute of Laser and System Technologies (iLAS), Denickestr. 17, 21073, Hamburg, Germany

ARTICLE INFO

Keywords:
Material model
Additive manufacturing
Laser powder bed fusion
Ti–6Al–4V
Thermo-physical properties
Mechanical properties

ABSTRACT

In the laser powder bed fusion of metals (PBF-LB/M), process simulation is a key factor to the optimization of the manufacturing process with reasonable amounts of resources. While the focus of research lies on the development of approaches to solve the problem of length scales when comparing the laser spot to a parts dimension, the conscientious modeling of the material applied provides an opportunity to increase the accuracy of computational studies with no significant increase in required computational resources. Within this study, a material model of the commonly used Ti–6Al–4V alloy for the thermo-mechanical process simulation at macro- and part-scale is developed. Data reported in the literature as well as own experimental work is assembled to a model consisting of constant and linear functions covering the whole temperature interval relevant for PBF-LB/M. Also, possible influencing factors on both thermal and mechanical properties are investigated.

1. Introduction

Additive Manufacturing (AM) gains importance in manufacturing at a high rate, experiencing double-digit market growth for most of the last 30 years [1]. This growth is made possible by the constant improvements in technologies and AM materials. Additionally, the growing demand of individualized parts or parts optimized in terms of functionality or weight is driving the development of AM technologies, especially in the medical, automotive, and aerospace industry [2]. As materials and manufacturing are expensive, modeling and simulation are playing a crucial role to supplement the traditional trial and error approaches for the design and optimization of materials and components [3].

In the laser powder bed fusion of metals (acronym PBF-LB/M according to ISO/ASTM 59201), one of the most used AM technologies also known as selective laser melting, a part is manufactured by consecutively adding a powder layer to a powder bed and melting selected areas of the layer by laser irradiation. Because of the great difference in scale when comparing the size of a part to the laser spot diameter (several centimeters vs. 60–120 μm), the exact modeling of a part's production with the goal of temperature and residual stress or distortion prediction would lead to kilometers of laser scan path. The high demand in regard of computational resources and time still poses a great challenge in modeling at the scale of a part [3].

While current efforts in research are made to reduce the computational requirements so that PBF-LB/M part-scale simulation can be used by design engineers without access to huge computing centers, each simplification results in a decrease in accuracy of the result. At the same time, little attention is given to the second centerpiece of a simulation besides the heat input modeling, the material model. Whereas a poor material model can lead to crucial errors in temperature and residual stress calculation, a well-compiled material model can significantly increase the accuracy of the calculation without any increased need for computational resources. Therefore, this study aims at the development of an accurate material model for the thermo-mechanical macro- and part-scale process simulation of PBF-LB/M.

The alloy Ti–6Al–4V is among the most important of the advanced materials that are key to improve the performance in aerospace and terrestrial systems [4]. The excellent combination of specific mechanical properties, low weight and particularly good corrosion behavior make this alloy suitable for high performance applications [5]. There are barriers to the broad application of Ti–6Al–4V, though, namely the comparatively high cost [4] as well as the prominent development of residual stresses during PBF-LB/M, making Ti–6Al–4V prone to cracking and distortion during the manufacturing process [6]. This is due to the formation mechanism, which is based on the temperature gradient [7]. As titanium alloys are characterized by a large melting range compared to steel or aluminum, steep temperature gradients develop during the processing by PBF-LB/M. It is therefore of specific interest to ensure

* Corresponding author.
E-mail address: katharina.bartsch@tuhh.de (K. Bartsch).

https://doi.org/10.1016/j.msea.2021.141237
Received 20 October 2020; Received in revised form 17 February 2021; Accepted 2 April 2021
Available online 6 April 2021

suitable processing conditions to prevent any quality issues due to distortion by process simulation. To enable this precise configuration of process parameters with respect to the individual part to be manufactured, a thorough material model of Ti–6Al–4V is essential.

Due to the complexity of a materials microstructure, the description of the materials behavior can be complex as well. While the knowledge in material science is constantly increasing, many processes are not yet fully understood. This concerns the temperature dependency of the material parameters due to the changes in the microstructure as well as the influence of the respective elements in the alloy and atmosphere. For Ti–6Al–4V, the oxygen content is known to significantly affect the mechanical properties of the produced part, and even the phase change temperatures [8–10].

Since there is no holistic material model yet to build on and many processes are yet to understand, the model of this work will rely on stepwise linear functions to describe the material properties with regard to the respective microstructural phases and temperatures, if not constant. The influence of oxygen is neglected since scarce work assessing its effect is available.

After a short introduction into the modeling of PBF-LB/M, the requirements for a material model, and the implementation in published studies, this paper is split in two main sections corresponding to the thermal and mechanical material properties, respectively. Here, data from the literature and own experimental work is used to compile the material model. Last, a short outlook on further research necessary to implement a reliable material model is given.

2. State of the art

In order to create concise numerical models, the subject of the modeling needs to be understood. To provide a foundation to the material model developed in this study, the PBF-LB/M process is described in Section 2.1. Based on the described procedure, the current approaches to modeling PBF-LB/M are summarized. Furthermore, the required material properties are determined and compared to the material models applied in published computational studies.

2.1. Laser powder bed fusion of metals (PBF-LB/M)

The process of creating a product via PBF-LB/M consists of seven main stages, as depicted in Fig. 1. Prior to the actual manufacturing, a CAD model of the product is created (step 1). Due to the geometrical freedom provided by PBF-LB/M, design methodologies such as topology optimization may be involved in finding the optimal design [1,11]. After the design, the digital model is processed to generate the machine files for the manufacturing (step 2). Here, parts are placed and orientated on the build platform. If necessary, support structures to support overhanging features, dissipate process-induced heat, and fixate the part in space are added. Finally, all geometries are sliced into layers and the scan vectors of the laser beam are generated. Those scan vectors, together with the process parameters such as laser power and scan velocity, are translated into machine code executable by the respective manufacturing system. Both step 1 and 2 may incorporate the use of process simulation to ensure manufacturability. Step 3 includes the file transfer to the manufacturing system as well as the preparation of the manufacturing, e.g. material supply and evacuation or flooding with process gas.

The actual manufacturing (step 4) is an iterative process of selectively scanning consecutive powder layers with a laser beam. First, powder is supplied by the powder container (step 4a, left container), which is then deposited as a layer with a specific height by a coating element (step 4b), e.g. a roller or blade. Remaining powder is collected by an overflow container (right container) to be able to reuse the powder. When the powder layer application is finished, the laser exposure takes place (step 4c). The laser is introduced into the build chamber by a scanner operating two mirrors to move the laser beam focus in the work plane. After the exposure the build platform as well as the overflow container is lowered, and the procedure starts over again until all geometries are manufactured.

For a finished product, some post-processing is necessary. The parts are removed from the manufacturing system (step 5), and since in PBF-LB/M the parts are built directly on the build platform, they are separated from the build platform by e.g. milling or electrical discharge machining (step 6). Prior to detachment, a stress-relief heat treatment may be needed to avoid distortion after the detachment due to the release of residual stresses. Finally, if support structures are involved in the manufacturing, those are removed as they do not belong to the actual part (step 7).

2.2. Modeling the PBF-LB/M process of Ti–6Al–4V

The difference in scale when comparing the size of a part to the laser spot diameter poses a great challenge for the exact modeling of a part's production with the goal of temperature and residual stress or distortion prediction. Consequently, four different scales of modeling have developed over time: micro-scale, meso-scale, macro-scale, and part-scale modeling. In micro-scale modeling, the development of the material's microstructure is evaluated. On the meso-scale, the powder particles are modeled individually, and together with a moving laser heat source, the melting of the powder as well as the fluid dynamics in the melt pool can be examined. Furthermore, by utilizing the assumption of a homogeneous medium as representation of the powder to avoid modeling the individual particles, single pass scans of the laser are examined without considering fluid dynamics. The macro-scale modeling is also based on

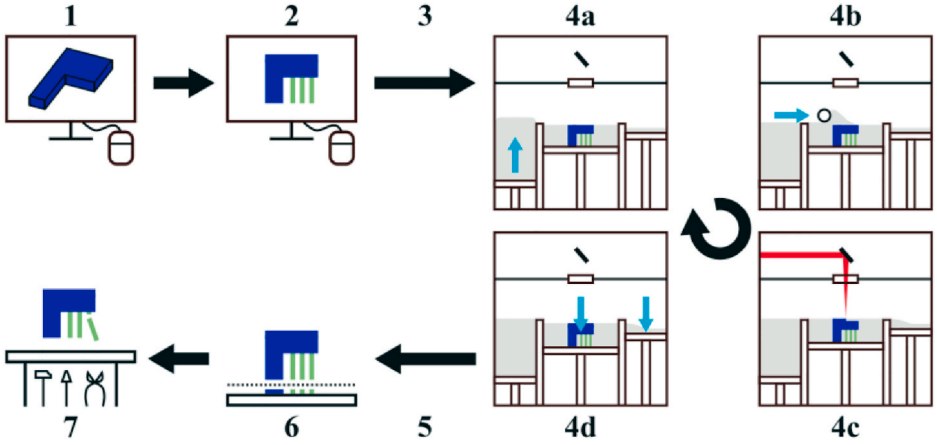

Fig. 1. Schematic process of PBF-LB/M.

the homogeneous medium assumption. Here, laser scan tracks up to a few whole layers (depending on area to be irradiated) are computed to investigate the effect of the heat input on a macroscopic material. When manufacturing a part by PBF-LB/M, several hundreds or thousands of layers are to be build, though, as the layer thickness ranges in the interval of 20 – 100 μm. Therefore, an even greater scale had to be developed. In part-scale modeling, the heat source is simplified by assuming uniform heat input to a whole layer or subset of it to avoid the small size of the laser spot. Depending on the size of a subset, one can acquire details about the temperature gradient in the build plane. However, the computational time increases accordingly, as the studies of Seidel et al. [12] and Chiumenti et al. [13] show in both their comparison of heat input models for PBF-LB/M part-scale simulation. To further reduce the overall amount of layers in part-scale modeling, several real layers are combined to one computational layer to reduce.

Most studies found in the literature focus on one scale in order to answer specific research questions. Especially in regard of the emerging concept of the digital twin, the coupling of those scales becomes increasingly important. The digital twin of a physical object consists of a digital representation of this object, where a bi-directional data flow between physical and digital object is enabled [14]. The digital object might include, but is not limited to numerical models of components or processes. A change in the physical object, e.g. recorded by integrated sensors, leads to a change of the digital object. At the same time, the digital object can act as controlling instance of the physical object, e.g. by adapting the process parameters in PBF-LB/M to the temperature in the part to be build when heat accumulation is detected during the manufacturing process. Given the increasing attention towards the digital twin in research and industry, numerical modeling is more important than ever. As the digital twin aims to entwine all process steps to one holistic framework, the coupling of the different scales is a precondition to the successful implementation of the digital twin. An approach towards the setup of a completely coupled modeling of PBF-LB/M has been presented by the Lawrence Livermore National Laboratory [3,15]. While the coupling of scales provides the opportunity to further understand the physics of the manufacturing process, it raises the challenge of an enormous demand of computational resources. In consequence, efficient modeling techniques are highly relevant. Here, precise material models are able to provide accuracy at little to no computational expense.

To thoroughly model materials for a specific manufacturing process, the underlying thermo-physical processes need to be identified (see Fig. 2). In PBF-LB/M, the manufacturing process starts with a single layer of powder material. Depending on the machine setup, the powder material is at room temperature or any temperature specified by a preheated build platform. With the start of the laser irradiation, the powder material is heated and finally molten. Evaporation may occur, but is avoided to reduce the risk of gas pores in the finished part. When the laser spot has passed the examined point in the material, the cooling phase begins. First, the material solidifies, and cools down to the ambient temperature of the build chamber. When the layer is finished, a new layer of powder material is deposited and the irradiation process is repeated. To achieve a complete bonding of the respective layers, process parameters are chosen in a way that the depth of the melt pool is up to three layers [16,17]. This means that the material will be remolten, and reheated even more times since the process-induced heat is conducted towards the build platform via the already solidified part geometry. In consequence, the material properties must be acquired for the solid, liquid, and powder form, taking temperature dependence into account. As powder material is not able to absorb mechanical forces, only the thermal properties need to be determined, though.

Throughout heating and cooling, material can change their microstructural phases. Ti–6Al–4V as a dual-phase α+β alloy transforms to a fully β-phase microstructure at elevated temperatures [9]. The temperature associated with the completion of this transformation process is called β-transus temperature (T_β). For most material processing technologies, Ti–6Al–4V transforms back into the α+β microstructure when cooled. In PBF-LB/M, the high cooling rates of over 10^6 K/s [18] typically result in the development of a fully martensitic (α') microstructure. The beginning of the transformation of the β-phase into the α'-phase is labeled by the martensite start temperature ($T_{\alpha'S}$). Each microstructural composition may have its own material behavior to be taken into account. See Fig. 2 for a complete overview of the temperature history and the respective material form of a specific point during PBF-LB/M.

Table 1 summarizes the individual material properties to be modeled for process simulation at macro- or part-scale, including the properties involved in the thermo-mechanical processes as well as the phase transitions, since they influence the aforementioned properties significantly. Besides T_β and $T_{\alpha'S}$, which are specific to the Ti–6Al–4V alloy, the liquidus temperature (T_l) – temperature above which the material will be liquid – and the solidus temperature (T_S) indicating the solidification

Table 1
Summary of Ti–6Al–4V material properties to be modeled in macro-scale process simulation of PBF-LB/M.

Thermo-physical properties			Mechanical properties		
β-transus temperature	T_β	[K]	Young's modulus	E	[GPa]
Solidus temperature	T_S	[K]	Yield stress	σ_Y	[MPa]
Liquidus temperature	T_l	[K]	Poisson's ratio	ν	[−]
(Evaporation temperature)	(T_e)	([K])	Coefficient of thermal expansion	*CTE*	[1/K]
α' start temperature	$T_{\alpha'S}$	[K]	(Ultimate tensile strength)	*(UTS)*	([MPa])
Density	ρ	[kg/m^3]			
Specific heat capacity	c_P	[J/(kgK)]			
Thermal conductivity	k	[W/(mK)]			
Absorption	a	[−]			

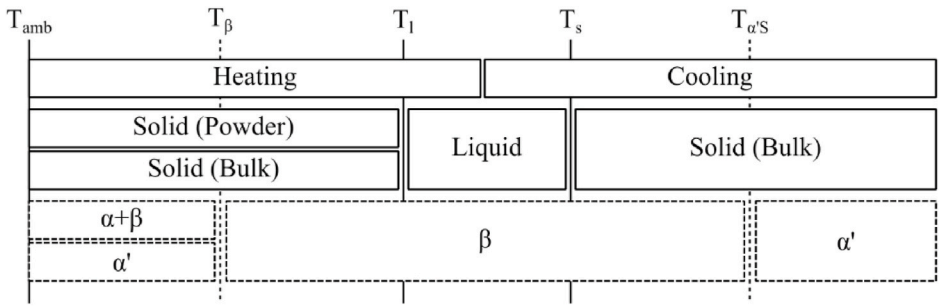

Fig. 2. Overview of temperature history, material form, and microstructure of a single Ti–6Al–4V layer processed by PBF-LB/M (left to right, dashed line: specific to Ti–6Al–4V).

of the material during cooling are essential temperatures to be known. The evaporation temperature (T_e) may also be useful to be known, though it is not necessarily reached. Further thermo-physical properties are the density (ρ) of the material, the specific heat capacity (c_P) describing the materials ability to taking energy in, and the thermal conductivity (k) indicating the materials ability to transmit heat. The absorption (a) denotes how much of the laser radiation is actually coupled into the material, not transmitted or reflected. To describe the mechanical behavior of the material, the Young's modulus (E) denotes the stiffness in the elastic material behavior, whereas the yield stress (σ_Y) labels the start of plastic deformation. The ultimate tensile strength (UTS) marks the maximum stress the material can bear without failure. This material property is not commonly applied in process simulation, but can help with the interpretation of the derived stresses. The Poisson's ratio (ν) indicates the expansion or contraction of the material perpendicular to the direction of loading. Finally, the coefficient of thermal expansion (CTE) describes the expansion of the material due to a change in temperature, coupling the thermal and mechanical physics.

Different ways to model the PBF-LB/M process at different scales may involve different materials properties. This is demonstrated in Table 2 and Table 3, which give an overview of computational studies modeling the PBF-LB/M process at various scales applying the Ti–6Al–4V alloy. Here, the modeled physics (T – thermal, TM – thermo-mechanical, M – mechanical) as well as the scale (MI – micro, ME – meso, MA – macro, PA – part) are indicated. Furthermore, the specified material properties are marked. The type of reference of the values is denoted by either "E" for experimental works or "S" for other PBF-LB/M simulations. The number prior to the letters shows the number of references given by the respective study. If no reference is indicated, it is marked with an "x". When the material property is modeled as temperature-dependent, "(T)" is added.

As can be seen from Table 2, only few publications consider all material properties noted in Table 1. Especially the Ti–6Al–4V specific temperatures $T_{\alpha'S}$ and T_β are attributed once and thrice, respectively. Note that there are studies not differentiating between T_S and T_l but give one value for the melting interval [20,34,35,38,40,41,43,44]. In this case, the melting temperature has been assigned as T_l in Table 2. Also, if the temperature-dependency of the material properties is considered, the key temperatures which are part of the heating process are indirectly modeled, even though no direct value is stated [36,37,39,45]. Furthermore, the powder material is modeled significantly less than the solid material. While powder property modeling is not necessary at the meso-scale when the powder particles are geometrically represented, the studies at macro- and part-scale apply the homogeneous medium assumption, which requires the assignment of effective powder material properties.

Beneath the question of which material properties are modeled in thermal PBF-LB/M process simulation, it is also important to evaluate the quality of the material modeling. In the field of specific

Table 3
Ti–6Al–4V material modeling in mechanical PBF-LB/M process simulation.

Source	Physics	Scale	E	σ_y	ν	CTE
[46]	M	MI	x(T)	x(T)		x(T)
[25]	TM	ME	2 ES(T)	2 ES(T)		2 ES(T)
[27]	TM	ME	1S(T)	1S(T)		1S(T)
[36]	TM	MA	2E(T)	2E(T)		2E(T)
[37]	TM	MA	1S(T)	1S(T)		1S(T)
38]	TM	MA	x(T)	x(T)		x(T)
[40]	TM	MA	1S(T)	1S(T)	1S(T)	1S(T)
[41]	TM	MA	1S(T)			
[39]	TM	MA	x(T)		x(T)	
[42]	TM	MA	1E(T)	1E(T)	2E(T)	1E(T)
[43]	TM	PA	x(T)	x(T)	x	x(T)
[45]	TM	PA	x(T)			x(T)
[47]	M	PA	1E(T)	1E(T)	1E(T)	1E(T)
[48]	M	PA	x	x	x	
[49]	M	PA	x(T)	x(T)	x(T)	x(T)

Physics: T – thermal, M – mechanical, TM – thermo-mechanicalScale: MI – micro, ME – meso, MA – macro, PA – partReference: x – no reference, E – experimental, S – simulation, number = number of references, (T) – temperature-dependency modeled.

Table 2
Ti–6Al–4V material modeling in thermal PBF-LB/M process simulation.

Source	Physics	Scale	T_β	T_S	T_l	T_e	$T_{\alpha'S}$	Powder Material				Solid Material			
								ρ	c_P	k	a	ρ	c_P	k	a
[19]	T	MI		1S	1S	1S						1S	1S(T)	1S(T)	1S
[20]	T	ME			x	x						x(T)	x(T)		x
[21]	T	ME		x	x							x(T)	x(T)	x(T)	x
[22]	T	ME	1S	1S	1S	1S		x(T)	x(T)	x(T)	1S	1S(T)	1S(T)	1S(T)	1S
[23]	T	ME		1S	1E					1S		1E(T)	1E(T)	1E(T)	
[24]	T	ME		1S	1S					1S(T)	3S	x(T)	x(T)	x(T)	1S
[25]	TM	ME		1E	1E							1E	1E(T)	1E(T)	
[26]	T	ME		x	x			1S(T)	1S(T)	1S(T)		1S(T)	1S(T)	1S(T)	x
[27]	TM	ME		3 ES	3 ES			2 ES		2 ES(T)		3 ES(T)	3 ES(T)	3 ES(T)	3 ES
[28]	T	ME		1E	1E	1E						1E	1E(T)	1E(T)	
[29]	T	ME		x	x			x(T)	1S(T)	2 ES(T)	1S	1E(T)	2E(T)	4E(T)	1E
[30]	T	ME		1E	1E	1E			x(T)	3 ES(T)			3 ES(T)	3 ES(T)	
[31]	T	ME		1E	1E	1E						1E(T)	1E(T)	1E(T)	x
[32]	T	ME		x	x							x			
[33]	T	ME		x	x	x				1E	1E			1E(T)	1E
[34]	T	MA			2E	2E					1E	2E	2E	2E	
[35]	T	MA			x	1E				1E		1E(T)		1E(T)	1E
[36]	TM	MA										2E(T)	2E(T)	2E(T)	
[37]	TM	MA								1S(T)		1S(T)	1S(T)	1S(T)	2E(T)
[38]	TM	MA			1S			1S(T)	1S(T)	2 ES(T)		1S(T)	1S(T)	1S(T)	
[39]	TM	MA						x(T)		x(T)		x(T)	x(T)	x(T)	
[40]	TM	MA	x		x		x	2E(T)		2E(T)		2E(T)		2E(T)	
[41]	TM	MA			x						1S	1S(T)	1S(T)	1S(T)	
[42]	TM	MA								x(T)				x(T)	
[43]	TM	PA	x		x	x			x(T)	x(T)		x(T)	x(T)	x(T)	x
[44]	T	PA			x	x			x(T)		1E	1S(T)	1S(T)	1S(T)	
[45]	TM	PA						1E(T)	1E(T)	1E(T)	x	1E(T)	1E(T)	1E(T)	

Physics: T – thermal, M – mechanical, TM – thermo-mechanical, Scale: MI – micro, ME – meso, MA – macro, PA – part, Reference: x – no reference, E – experimental, S – simulation, number = number of references, (T) – temperature-dependency modeled.

temperatures, often no reference is given. This occurs for the thermal properties, too, but not as frequent. Additionally, the number of references per material property or even material property set is low, only few studies denote more than one reference [27,29,30,34,40]. As shown in Section 3, different experimental studies can produce a wide range in values for the same material property, because the actual material configuration as well as the experimental method influence the results. Using one specific reference based on a single dataset can therefore induce deviations in the result. With regard to the type of reference, 12 out of 21 publications use other PBF-LB/M process simulations as reference, whereas 15 works employ experimental studies. In Refs. [23,29,37,44], both reference types are applied. Saxena et al. [27], Fu & Guo [30], and Zhao et al. [38] even mix experimental and computational references for one specific material property. The extensive use of non-experimental data sources may be due to the small number of experimental studies available (see Section 3), but bears the risk of transmission errors.

In the field of mechanical PBF-LB/M simulations, Table 3 reveals a smaller number of computational studies compared to the thermal modeling of the PBF-LB/M process. The studies presented act mainly on the macro- and part-scale, while in thermal modeling the focus is shifted towards the meso-scale. Most studies rely on the coupling of both physics, but Rangaswamy et al. [46], Li et al. [47], Ahmad et al. [48], and Chen et al. [49] apply other methods such as the inherent strain method to compute the residual stresses while not considering the thermal aspects of the process directly. Because the powder material in PBF-LB/M is not able to transfer mechanical loads as the movement of the particles is not restricted in all directions, there is no need to experimentally investigate mechanical powder properties. Compared to Table 2, a higher density in referenced material properties is noticeable. Still, a relatively high number of studies not referencing their material model remains. The involvement of a high number of computational studies as references is also matched. Except for Ahmad et al. [48], all studies include the dependency on the temperature.

A critical point in the modeling of the mechanical material properties found in the studies presented in Table 3 is the material processing in the experimental references. Here, only alloys processed by conventional technologies are investigated. The martensitic microstructure evolving because of the high cooling rate heavily affects the mechanical properties. It is therefore of special importance to assemble a mechanical material model based on experimental work done with PBF-LB/M specimen.

In summary, the following issues have been identified in the current way of Ti–6Al–4V material modeling in PBF-LB/M process simulation:

1. In thermal modeling, due to the variety in numerical approaches, no consistent material model is available as different requirements regarding the considered material properties exist. Also, microstructural phase change is often neglected.
2. A considerable amount of computational studies does not provide references for their material model.
3. Only a small number of references is included, neglecting the variation of data.
4. A significant amount of referencing to other computational studies takes place, inducing the risk of transmission errors.

To exploit the potential of material modeling in terms of computational accuracy, the development of a concise material model explicitly for the PBF-LB/M process is crucial. The presented works aims to create a starting point for the development of such a material model.

3. Thermo-physical properties of Ti–6Al–4V

For the modeling of the thermo-physical properties of Ti–6Al–4V, an extensive literature review of experimental works is conducted and summarized in Table 4. For properties highly dependent on the microstructure, the literature data is supplemented by own experimental work. The goal here is to investigate the influence of the martensitic microstructure found in PBF-LB/M Ti–6Al–4V compared to the usual (α+β)-microstructure. To model the material properties, either the median is calculated, if there is no temperature dependency, or the available data is fitted by linear functions. Most thermo-physical properties will not exactly be represented by a piecewise linear function, as can be seen in the following figures, because there are more influencing factors than the temperature. Those influencing factors are not completely known yet, let alone reported in the literature available. As a consequence, the authors decided to stick with linear functions, which are also easily handled by a computational solver.

Table 4
Literature overview of experimental work on thermo-physical properties of conventionally processed Ti–6Al–4V.

Source	T_β	T_S	T_l	T_e	$T_{\alpha'S}$	ρ	c_P	k	a
[50]	(x)				(x)				
[51]					(x)				
[52]						x			
[53]									x
[54]									x[a]
[55]									x
[56]									x
[57]									x
[58]			x			x	x		
[59]					x				
[60]	x	x	x				x	x	
[61]									x
[62]	x		x				x		
[9]	x				x				
[10]	x						x	x	
[63]							x		
[64]	x		x			x	x	x	
[65]	x				x				
[66]	x								
[67]		x	x				(x)		
[68]	x								
[69]							x	x	
[70]	x		x				x		
[71]								x	
[72]	x		x				x	x	

[a] Data for powder material only (x) referenced data.

3.1. β-transus temperature

For T_β, there is a relatively high number of values given in the literature, compared to the other thermal properties displayed in Table 4. The data covers a wide range from 1160 K [62] to 1300 K [70], and is obtained testing conventionally manufactured Ti–6Al–4V with an α+β microstructure. The difference in the experimental values may be due to variances in the composition of the alloying elements, as the standard specifications (ASTM B248, ASTM B348) do allow for 5.5–6.75 wt% aluminum and 3.5–4.5 wt% vanadium. The alloying elements act as phase stabilizers (aluminum as α-stabilizer, vanadium as β-stabilizer [13]), heavily influencing T_β. Furthermore, the oxygen, nitrogen, and carbon content as α-stabilizers affect T_β [8–10]. Because the microstructure of PBF-LB/M Ti–6Al–4V differs from the conventional α+β microstructure, Differential Scanning Calorimetry (DSC) with PBF-LB/M specimens is performed for additional data on Ti–6Al–4V with martensitic microstructure.

3.1.1. Experimental Setup

A cube with an edge length of 10 mm is manufactured with a SLM500HL system (SLM Solutions AG, Lübeck, Germany) under argon atmosphere with a laser power of 240 W, a scan velocity of 1200 mm/s, a layer thickness of 60 µm, and a hatch distance of 105 µm. Powder material (Tekna Advanced Materials Inc., Sherbrooke, Canada) with a particle size distribution of 23-50 µm is used. To fit the DSC equipment

(TGA/DSC 2 HT 1600, Mettler-Toledo AG, Schwerzenbach, Switzerland) and eliminate any influence of the surface roughness, the cube is cut into smaller cubes by dividing it in three along each dimensional axis via wire electrical discharge machining (EDM). The center cube is then subjected to the heating and cooling sequence presented in Table 5. As the behavior of α'-Ti-6Al–4V is not known, but expected to be similar to the (α+β)-Ti-6Al–4V, the target temperature interval of 1073 – 1473 K is chosen so that the actual phase transition will not be missed and fully completed. Additionally, a heating step prior to the target temperature interval is included to adjust the specimen to the reduced heat rate. The measurements are conducted under argon atmosphere to prevent oxidation to alter the measurements. The heat rate of ±50 K/min is chosen according to Gadeev & Illarionov [74] as a compromise of the fast heating necessary for the evaluation of high-alloyed materials and receiving a reasonable signal during measurements. This heat rate does not match the rapid heating in PBF-LB/M, which can be in the order of 10^5 to 10^7 K/s [51,73] and cannot be captured using current DSC technology. However, the high heating and cooling rates characteristic for PBF-LB/M occur only in the small zone of molten material and its adjacent volume. Further away, the heat conduction slows down. Therefore, the values obtained in this experiment may not be completely representative for the first few layers, but are valid in the region of the already solidified layers who are still reheated several times due to the heat dissipation from the first layers to the build platform.

3.1.2. Results of DSC for T_β determination

The result of the DSC is presented in Fig. 3 and Fig. 4 for the heating and cooling steps, respectively. The procedure of Gadeev & Illarionov [74] is applied to determine T_β. Gadeev & Illarionov propose to utilize the derivative maximum temperature, based on the observation of the low intensity of the thermal effect compared to e.g. polymorphic transformation:

$$T_\beta = \max(dT) - f_c \pm 1 \quad (1)$$

They included a correction factor (f_c), which is determined experimentally and related to the molybdenum equivalent $[Mo]_{eq}$ of an alloy.

$$f_c = -1.63*[Mo]_{eq} + 20.14 \quad (2)$$

For Ti–6Al–4V, $[Mo]_{eq}$ is determined to equal 3 [74]. The result of both data sets for T_β is calculated and presented in Fig. 5, together with the literature data. The experimental values for T_β are in good agreement with the data obtained by other studies. The experimental determination of T_β is sensitive to the heat rate as the material's response and the measured signal are slightly delayed [65], resulting in a range of values as seen in Fig. 5, where the values of the studies displayed in Table 4 are shown. The experimental values accumulate around 1268 K, though. Finally, to determine T_β the median of both experimental and literature data is calculated, yielding T_β = 1268 K, also.

3.2. Liquidus temperature

Slightly less values for the liquidus temperature T_l are found in the literature (see Table 4), compared to T_β. Fig. 6 presents the distribution of those, and a tendency to either 1923 K [60,64,72] or 1943 K [58,62,70] becomes apparent. As the material will reach T_l with a β-phase microstructure no matter the manufacturing process, no additional experiment is conducted. The median of the data is considered, giving T_l = 1928 K [67].

Table 5
Heating/Cooling sequence of DSC experiment (T_β).

Step	Temperature	Heat rate	Argon flow rate
1	298 – 973 K	100 K/min	20 ml/min
2	973 – 1073 K	50 K/min	20 ml/min
3	1073 – 1473 K	50 K/min	20 ml/min
4	1473 – 1073 K	−50 K/min	20 ml/min
5	1073 – 298 K	−100 K/min	20 ml/min

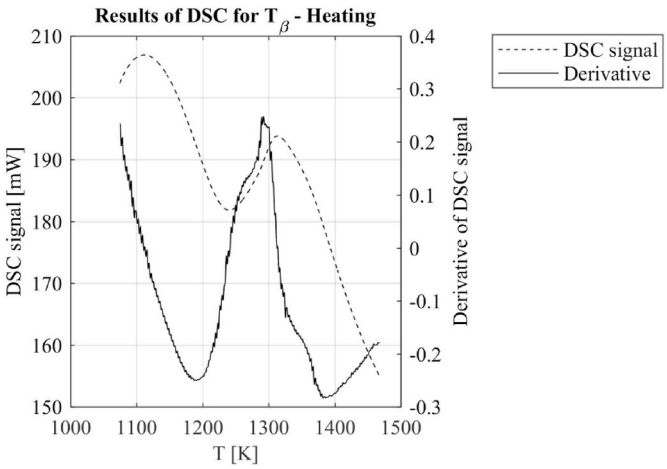

Fig. 3. DSC signal and its derivative for the heating sequence.

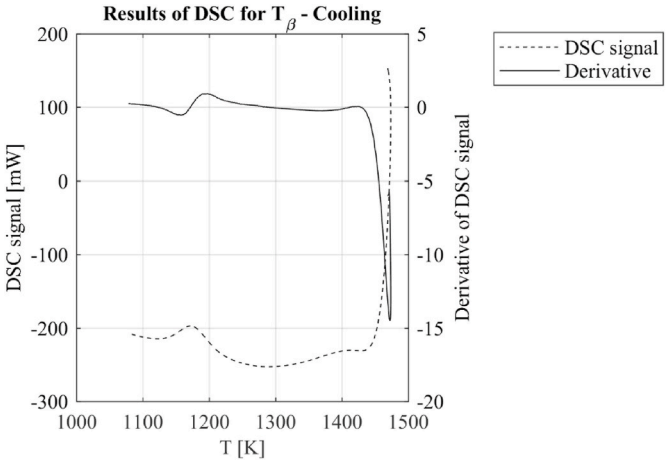

Fig. 4. DSC signal and its derivative for the cooling sequence.

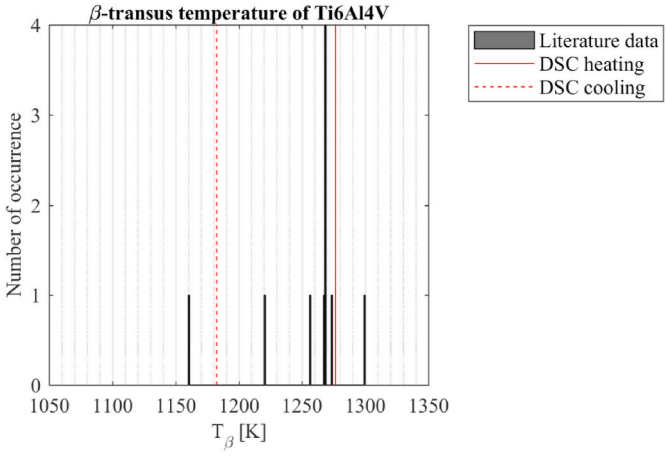

Fig. 5. Data for T_β from DSC as well as literature.

3.3. Solidus temperature

Only two references for T_S are found in the literature evaluated in

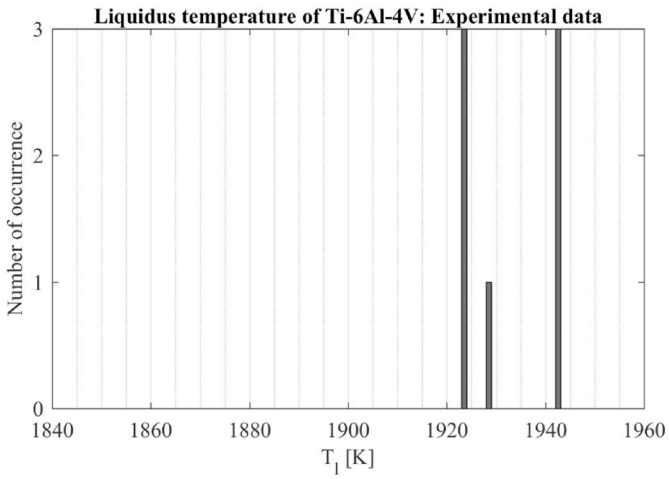

Fig. 6. Literature data for T_L.

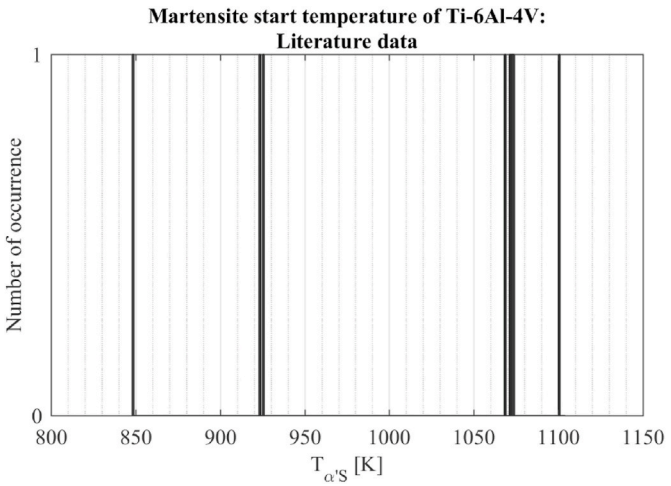

Fig. 8. Literature data for $T_{\alpha'S}$.

Table 4, proposing $T_S = 1873$ K [25] or $T_S = 1878$ K [33]. Because this data set is considered too small for a reasonable evaluation, values given for T_S in published PBF-LB/M process simulations [19–33] as well as other related manufacturing processes simulations such as direct energy deposition (DED) [75–79], electron beam powder bed fusion [80–82], and laser welding [83,84] are added. The created data set is displayed in Fig. 7. A strong tendency towards 1878 K is noticed, which is affirmed by the median of the data set. Similar to the determination of T_l, no further experimental work is done. The median is taken as final value, yielding $T_S = 1878$ K.

3.4. Martensite start temperature

For $T_{\alpha'S}$, some experimental studies have been conducted, as shown by Table 4. Furthermore, Neelakatan et al. [59] derived a formula to predict $T_{\alpha'S}$ for β-Ti alloys based on their composition expressed in terms of the elemental concentrations:

$$T_{\alpha'S} = 1156[\mathrm{K}] - 150\mathrm{Fe}_{\mathrm{wt.\%}}\,[\mathrm{K}] - 96\mathrm{Cr}_{\mathrm{wt.\%}}\,[\mathrm{K}] - 49\mathrm{Mo}_{\mathrm{wt.\%}}\,[\mathrm{K}] - 37\mathrm{V}_{\mathrm{wt.\%}}\,[\mathrm{K}] - 17\mathrm{Nb}_{\mathrm{wt.\%}}\,[\mathrm{K}] - 7\mathrm{Zr}_{\mathrm{wt.\%}}\,[\mathrm{K}] + 15\mathrm{Al}_{\mathrm{wt.\%}}\,[\mathrm{K}] \quad (3)$$

For Ti–6Al–4V, only Fe, V, and Al contribute to this formula. Four experimentally measured chemical compositions of Ti–6Al–4V are applied to generate more data by using Equation (3): 6.39Al4.08V0.19Fe [8], 6.5Al4.06V0.21Fe [8], 6.27Al4.1V0.2Fe [8], and 5.5Al3.5V0.03Fe [64]. The resulting data set is displayed in Fig. 8. The seemingly varying thickness of the bars indicate the existence of contiguous values. Fig. 8 also demonstrates the dependence of $T_{\alpha'S}$ on the cooling rate [65], resulting in the large range of 848 K [65] to 1104.5 K [59] Since the cooling rate of PBF-LB/M has only been estimated, the median of the data set is considered, yielding $T_{\alpha'S} = 1073$ K.

3.5. Evaporation temperature

No experimental data has been found by the authors for T_e. To give an orientation, the values applied in published PBF-LB/M and other related manufacturing process simulations [19,20,22,28,34,35,43,44,77,83–85], are examined and presented in Fig. 9. T_e is subject to the largest range of values, with a minimum value of 3133 K [83] and a maximum value of 3613 K [19]. In accordance to the procedure to determine a model value for a specific temperature applied in the previous sections, the median is considered, giving $T_e = 3533$ K.

3.6. Density

While the density at room temperature of Ti–6Al–4V is well known, specifications in material data sheets ranging from 4410 kg/m^3 (EOS GmbH, 2017) to 4430 kg/m^3 (SLM Solutions AG, 2020), the density at higher temperatures has not received much attention in research, as indicated by Table 4 and Fig. 10. One reason might be that most computational studies do not model the material shrinkage or expansion, and therefore have to fix the density at a constant value.

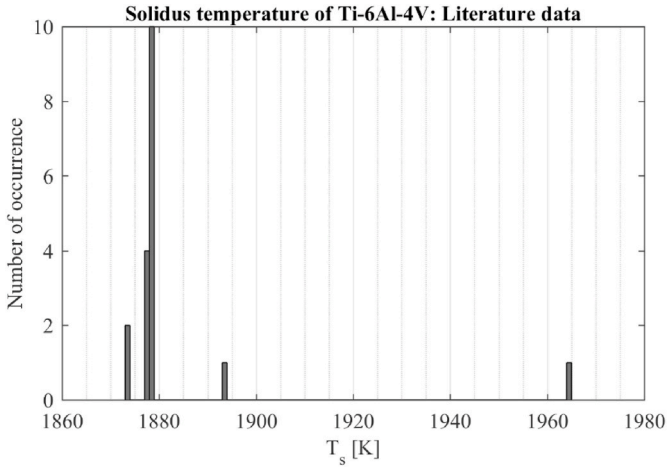

Fig. 7. Literature data (experimental and computational studies) for T_S.

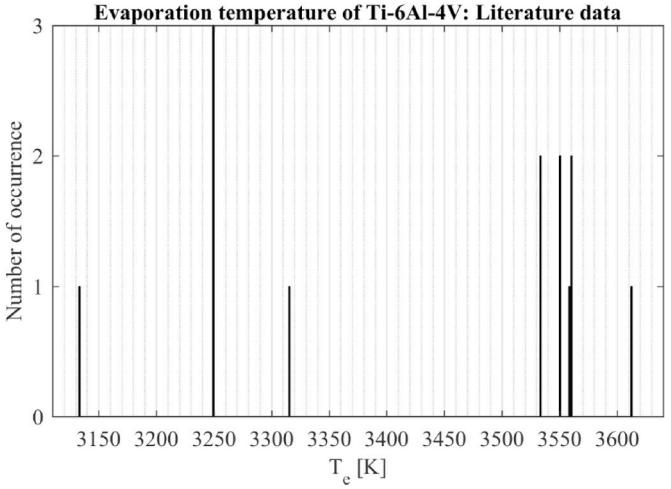

Fig. 9. Literature data of computational studies for T_E.

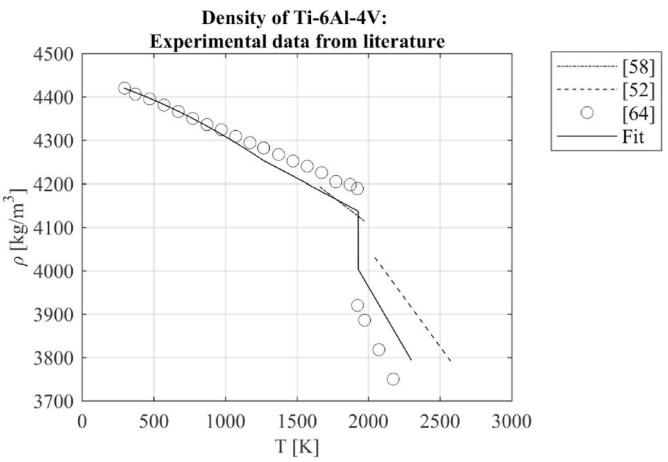

Fig. 10. Result of the fitting procedure for the modeling of the density.

Furthermore, the measurement of the density at higher temperatures remains difficult and is prone to errors. The coefficient of thermal expansion *CTE* is directly linked to the density, though. To keep the material model presented in this work consistent, the density is calculated from the *CTE* model presented in Section 4.5.

The term 'coefficient of thermal expansion' is commonly used for the coefficient of linear thermal expansion (*CLTE*), i.e. the material's change in one dimension. Extending the *CTE* to further dimensions, there are also the coefficient of area thermal expansion (*CATE*) for the 2D case, and the coefficient of volume thermal expansion (*CVTE*), which can be derived from the change in ρ. For the *CVTE*, the following rule applies [86]:

$$CVTE = 1/V * dV/dT \tag{4}$$

Here, V denotes the volume of the solid, and T the temperature in °C. Since V can be expressed by the mass m and the density ρ, and m is assumed constant, Equation (4) can be written as

$$CVTE = 1/\rho * d\rho/dT \tag{5}$$

There is a linear relationship between *CTE* and *CVTE*, based on the number of dimensions [86]:

$$CVTE = 3*CTE \tag{6}$$

Solving Equation (5) for ρ after transforming *CTE* to *CVTE* and evaluating it stepwise with the model of *CTE* presented in this work (cf. Section 4.5) and an initial density of 4420 kg/m^3 at room temperature, the following description of ρ is determined:

$$\rho_{\alpha'}(T) = -5.13*10^{-5}\ [kg/m^3]\ *T^2/[K^2] - 0.01935\ [kg/m^3]\ *T/[K] + 4451\ [kg/m^3] \tag{7}$$

$$\rho_{\beta}(T) = -2.762*10^{-6}\ [kg/m^3]\ *T^2/[K^2] - 0.1663\ [kg/m^3]\ *T/[K] + 4468\ [kg/m^3] \tag{8}$$

The experimental data of the literature as well as the fits are shown in Fig. 10. It is noticed that no significant change in density occurs at the phase transition to the β microstructure. This is in good agreement with literature, as the density difference of Ti (hcp) and Ti (bcc) is $\Delta\rho << 1\%$ based on the calculation of the volumes of the respective unit cells using the lattice constants from Wood [87] and Levinger [88], which can be superimposed on the α/α' (hcp) + β (bcc) microstructure of Ti–6Al–4V.

Because of the high heating rates in PBF-LB/M, the model presented in this work does not include an exact description of the so-called "mushy zone" in the temperature interval of $T_S < T < T_L$, where solid and liquid phases coexist during melting. Due to missing data on the *CTE* of liquid Ti–6Al–4V, the data of Mills [64] and Schmon et al. [53] is linearly fit:

$$\rho_l\ (T) = -0.565\ [kg/m^3]\ *T/[K] + 5093\ [kg/m^3] \tag{9}$$

Schmon et al. [53] found a significant drop in the density above 2500 K. The most obvious explanation for this drop would be the material state transition to vapor. The value of 2500 K does not coincide with the data reported for T_e (cf. Section 3.5), but is close to the evaporation temperature of aluminum, which is around 2743 K [89]. It is therefore concluded, that the evaporation of aluminum is the reason for the drop. As there are two measurement values only and the definite loss of material is not modeled in computational studies at macro-scale, the whole liquid phase is modeled with the data of Schmon et al. [53] below 2500 K. To give a complete material model including both heating and cooling of the material, Table 6 summarizes the respective temperature intervals according to Section 2 as well as the corresponding function.

3.7. Specific heat capacity

The specific heat capacity describes the heating and phase change of a certain material, and is highly dependent on the materials temperature. Fig. 11 displays different experimental studies and their results with regard to c_P of conventionally processed Ti–6Al–4V. It is immediately noticed that there is a high variance in the values, with a maximum of nearly 300 J/(kg*K) at around 1200 K. This is due to some experimental results exhibiting a peak at T_β while others do not. The explanation lies within the measurement methods applied. The peak for c_P is an artificial one caused by the phase transformation. The energy is not used to raise the materials temperature as indicated by c_P, but operates the phase transformation. When applying measurement methods that are based on an energy difference such as pulse heating [60,62], it is not possible to distinguish between actual heat capacity and phase transformation. This relationship between c_P and phase transformation is used to indirectly model phase transformations and their enthalpies via the apparent (heat) capacity approach, which Proell et al. [90] found to be equally efficient in comparison with the more advanced heat integration method. Here, the phase change enthalpy is included like it can be seen in the experimental data as well, either as peak or valley.

Fig. 11 also demonstrates that phase transformations lead to a discontinuity in the c_P development over temperature: At T_β, c_P drops while increasing at T_l. Consequently, these discontinuities have to be included in the final model of c_P. For PBF-LB/M, the model of c_P consists of three sections corresponding to the α'-microstructure, the β-microstructure as well as the liquid phase. Each section is represented by a linear function and an additional term for the phase transitions. As the microstructure of the material may influence c_P, and the experimental data available is obtained on (α+β)-microstructure, own experimental work is conducted in order to investigate whether there is a significant difference to the martensitic microstructure characteristic for PBF-LB/M.

3.7.1. Experimental Setup

To obtain data on c_P, Differential Scanning Calorimetry (DSC) is used, see section 3.1.1 for the experimental equipment. Two specimens manufactured by the conditions described in section 3.1.1 are subjected to the same thermal cycle (see Table 7) twice. Again, argon is used as a protective gas to prevent oxidation. Since the maximum temperature

Table 6
Material model of Ti–6Al–4V – Density, functions and temperature intervals for one full temperature cycle (upper section: heating, lower section: cooling).

Temperature	Microstructural phase	Function
$T_R < T <= T_\beta$	α'	$\rho_{\alpha'}\ (T)$
$T_\beta < T <= T_L$	β	$\rho_\beta\ (T)$
$T_L < T$	liquid	$\rho_l\ (T)$
$T_S < T$	liquid	$\rho_l\ (T)$
$T_{\alpha'S} < T <= T_S$	β	$\rho_\beta\ (T)$
$T_R < T <= T_{\alpha'S}$	α'	$\rho_{\alpha'}\ (T)$

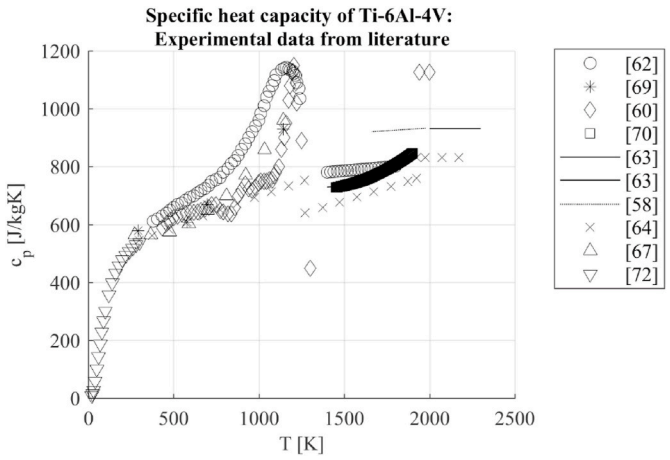

Fig. 11. Experimental data from literature for the specific heat capacity.

Table 7
Heating/Cooling sequence of DSC experiment (c_P).

Step	Temperature	Heat rate	Argon flow rate
1	293 K	(hold for 30 min)	20 ml/min
2	293 – 1573 K	50 K/min	20 ml/min
3	1573 – 298 K	−50 K/min	20 ml/min
4	298 K	(hold for 5 min)	20 ml/min

during the heating exceeds T_β significantly, the specimens will have a α'-microstructure in the first run, but a (α+β)-microstructure in the second run due to the low cooling rate. As the same specimens are investigated, any influences of the manufacturing process are avoided in the direct comparison of the results.

3.7.2. Results of DSC for c_P evaluation

The corresponding curves of the measured signals are displayed in Fig. 12. Up until 1073K, both curves for the respective microstructures are in parallel, but diverge when the phase transformation takes place (indicated by the drop in heat flow), which is why Fig. 12 puts emphasis on this temperature interval. The overall DSC signal is characterized by two maxima with a minimum between them. While the difference of the curves is 6 mW at 883 K and 5 mW at the first maximum (1127 K for α', 1131 K for α+β), it increases to 9 mW at 1233 K (minimum of α'), 20 mW at 1274 K (minimum of α+β), and finally 30 mW at the second maximum (1323 K for both α+β and α'). Interestingly, the second maximum denoting the end of the phase transition is taking place at the same temperature, in contrast to the prior peak and valley, which are slightly offset to each other. This is due to the fact that martensite as a metastable phase decomposes more easily than the (α+β)-microstructure. Up until the β-transus temperature determined in Section 3.1, the difference between the α'- and (α+β)-signal is ca. 5% or lower in regard to the (α+β)-signal. It is therefore concluded, that the two microstructures do behave similar with regard to c_P.

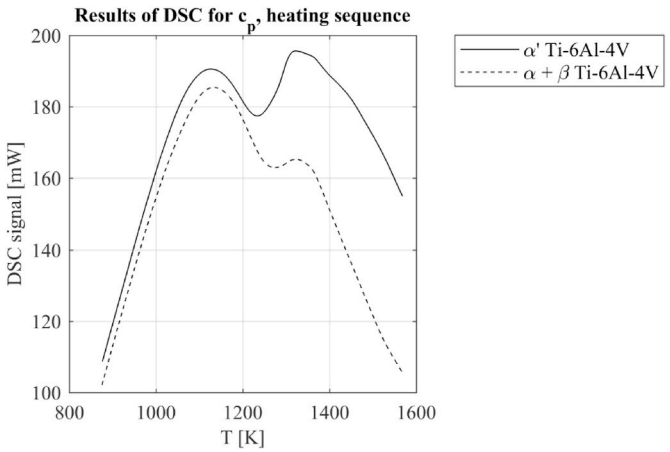

Fig. 12. Results of DSC for c_p, displaying the heating sequence.

3.7.3. Modeling of c_P

For the first section with $T_R < T <= T_\beta$, the experimental data reported in the literature is fitted to

$$c_{p,\alpha',lin}\,(T) = 0.25\ [\mathrm{J/(kgK)}]\ *T/[\mathrm{K}] + 483\ [\mathrm{J/(kgK)}] \tag{10}$$

As no specification on the enthalpy of the β-transus could be found by the authors, the experimental data shown in Fig. 11 is also used to determine the term for the phase change. Here, a standard Gaussian distribution function is applied:

$$c_{p,\alpha',heat,phase}\,(T) = 13{,}000\ [\mathrm{J/(kgK)}]\ *(1/90*\mathrm{sqrt}(2*\mathrm{pi}))*\exp(-0.5*((T/[\mathrm{K}] -1160)/90)\text{^}2) \tag{11}$$

The result of the fitting procedure with $c_{p,\alpha',heat}\,(T) = c_{p,\alpha',lin}\,(T) + c_{p,\alpha',heat,phase}\,(T)$ is presented in Fig. 13. The same procedure is applied to the second section of $T_\beta < T <= T_l$. First, the actual material property is fitted by a linear function:

$$c_{p,\beta,lin}\,(T) = 0.14\ [\mathrm{J/(kgK)}]\ *T/[\mathrm{K}] + 530\ [\mathrm{J/(kgK)}] \tag{12}$$

In the second step, the phase transformation is modeled. For the latent heat of fusion, few values of 286 kJ/kg [68], 290 kJ/kg [60], and 300 kJ/kg [58] are given in the literature. The value of Boivineau et al. [60] is chosen as the median of those. Now, the Gaussian distribution function is applied to the temperature interval of 50 K, ending at T_l, such that the area between the distribution function and the linear material function equals the latent heat of fusion.

$$c_{p,\beta,heat,phase}\,(T) = 41{,}650\ [\mathrm{J/(kgK)}]\ *(1/9*\mathrm{sqrt}(2*\mathrm{pi}))*\exp(-0.5*((T/[\mathrm{K}] -1905)/9)\text{^}2) \tag{13}$$

Again, the sum of both terms $c_{p,\beta,lin}\,(T)$ and $c_{p,\beta,heat,phase}\,(T)$ yield the overall specific heat capacity of this section, $c_{p,\beta,heat}\,(T)$. In the liquid material state, c_p is found to be constant by Kaschnitz et al. [63], Mills [64], and Boivineau et al. [60]. Determining the median of the reported values, this third section is described as

$$c_{p,l}\,(T) = 930\ [\mathrm{J/(kgK)}] \tag{14}$$

The result of the literature data fitting is shown in Fig. 14, without the phase transformation terms as the height of the latent heat of fusion

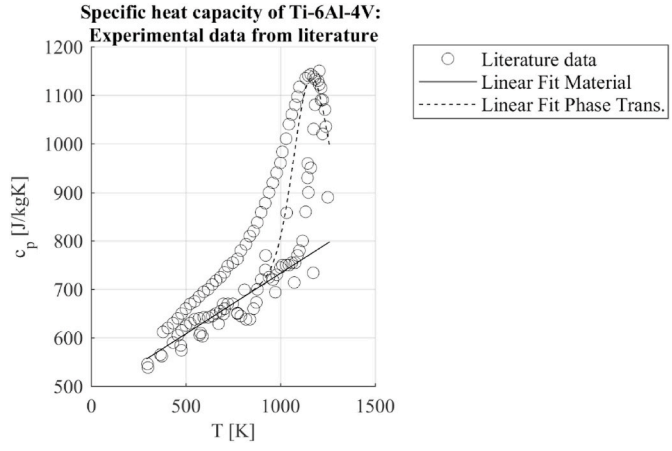

Fig. 13. Result of the fitting procedure (first section) for the modeling of the specific heat capacity.

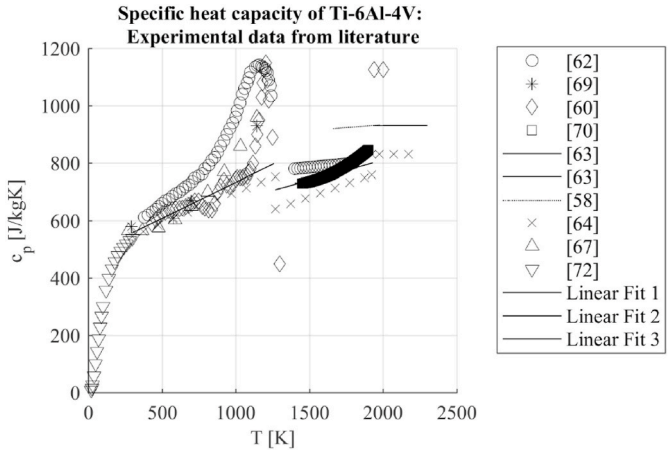

Fig. 14. Result of the fitting procedure for the modeling of the specific heat capacity.

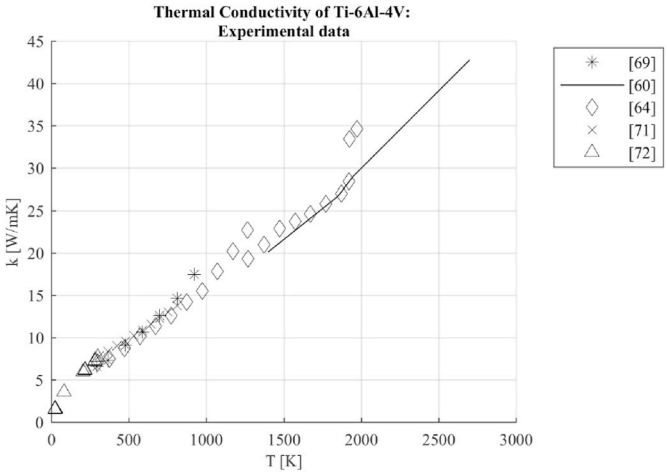

Fig. 15. Experimental data from the literature for the thermal conductivity.

peak would make it impossible to notice anything in the remaining figure. For the cooling of the material, the functions of the phase transformations have to be adjusted to the new temperature intervals with regard to T_s and $T_{\alpha's}$.

$$c_{p,\alpha',cool,phase}\ (T) = 13{,}000\ [J/(kgK)] * (1/90*sqrt(2*pi))*exp(-0.5*((T/[K] -952)/90)^2) \quad (15)$$

$$c_{p,\beta,cool,phase}\ (T) = 41{,}650\ [J/(kgK)] * (1/9*sqrt(2*pi))*exp(-0.5*((T/[K] -1855)/9)^2) \quad (16)$$

While the phase transformation of the heating cycle is an endothermic process, the cooling cycle has an exothermic behavior, consequently. Therefore, the overall specific heat capacity is described by

$$c_{p,\alpha',cool}\ (T) = c_{p,\alpha',lin}\ (T) - c_{p,\alpha',cool,phase}\ (T) \quad (17)$$

$$c_{p,\beta,cool}\ (T) = c_{p,\beta,lin}\ (T) - c_{p,\beta,cool,phase}\ (T) \quad (18)$$

Table 8 summarizes the functions of the specific heat capacity's model with regard to the temperature intervals defined in Section 2.

3.8. Thermal conductivity

The experimental data reported according to Table 4 is presented in Fig. 15. Two important aspects are noticed: On the one hand, the experimental data indicates a linear development of k with increasing temperature. On the other hand, similar to c_p, discontinuities at the phase transformation points as well as different slopes of the sections corresponding to the respective microstructures are identified. Accordingly, it is examined experimentally whether the α'-microstructure exhibits values for k similar to the (α+β)-microstructure.

3.8.1. Experimental setup

For the determination of the thermal conductivity, Laser Flash Analysis (LFA) is used. Cylinders with a diameter of 12.7 mm are manufactured with the help of an SLM500HL system (SLM Solutions AG, Lübeck, Germany) under argon atmosphere with a laser power of 240 W, a scan velocity of 1200 mm/s, and a hatch distance of 100 µm to fit the LFA equipment (Linseis LFA 1600, Linseis Messgeräte GmbH, Selb, Germany), each cylinder is cut into 12 discs with a target thickness of 2 mm, as the LFA equipment features a revolver sample holder allowing for six specimens to be measured in the same run. Prior to the experiments, the discs are coated with a graphite spray and the actual thicknesses are measured.

First, measurements at room temperature of both cylinder's specimens are conducted to investigate whether there is any influence of the manufacturing system. Because the sensor of the LFA are highly sensitive to its and the specimen's temperature, the measurements at one specimen are repeated five times. The measurements are performed under vacuum with a pressure $p < 2*10^{-3}$ hPa. For the laser pulse, the parameters of the iris sitting in front of the optic (I), the amplification factor (A) and the voltage (V) of the pulse have to be set. At T_R, $I = 2$, $A = 50$, and $V = 500$ V for the specimen of cylinder 1 and V = 400 V for the specimen of cylinder 2 is determined after a reference run. In a second experimental series, the dependence of k on the temperature is investigated for both α'- and (α+β)-microstructure. Here, the same specimens are subjected to measurements at temperatures up to 1423 K. Similar to the procedure for the modeling of c_p, the excess of T_β in combination with a low cooling rate will result in different microstructures in both runs. The laser pulse parameters are given in Table 9.

3.8.2. Experimental results of the Laser Flash Analysis

The comparison of the specimens cut from two different cylinders is shown in Fig. 16, displaying the thermal diffusivity d (usually denoted by α or a, changed for better distinction from the absorptivity), as this is the parameter originally measured by LFA. Additionally, the mean value of d at the respective temperature levels as well as the linear fit of the data is indicated. It can be seen, that the mean values are close to the linear fit and well within the standard deviation range of the experimental data. It is therefore concluded, that no significant influence of the manufacturing process has to be taken into account, and that data

Table 8
Material model of Ti–6Al–4V –Specific heat capacity, functions and temperature intervals for one full temperature cycle (upper section: heating, lower section: cooling).

Temperature	Microstructural phase	Function
$T_R < T <= T_\beta$	α'	$c_{p,\alpha',heat}\ (T)$
$T_\beta < T <= T_L$	β	$c_{p,\beta,heat}\ (T)$
$T_L < T$	liquid	$c_{p,l}\ (T)$
$T_S < T$	liquid	$c_{p,l}\ (T)$
$T_{\alpha'S} < T <= T_S$	β	$c_{p,\beta,cool}\ (T)$
$T_R < T <= T_{\alpha'S}$	α'	$c_{p,\alpha',cool}\ (T)$

Table 9
Laser pulse parameter used for the high temperature measurements.

T [K]		373	473	573	773	973	1173	1423
α'	I [−]	2	2	2	2	4	4	8
	A [−]	20	10	5	5	10	10	10
	V [V]	300	250	240	200	240	220	400
α+β	I [−]	2	2	2	2	4	4	8
	A [−]	50	20	10	2	5	2	5
	V [V]	400	280	250	250	250	300	30

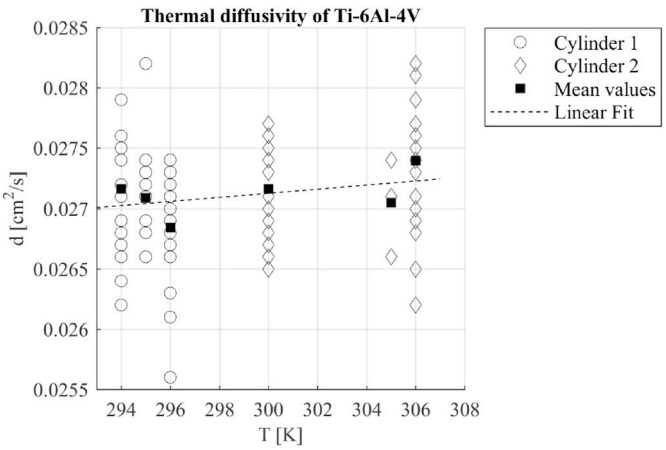

Fig. 16. Experimental results of LFA for the comparison of different base cylinders.

obtained from one cylinder is representative for the other cylinder as well.

Based on the observations made in the first experimental series, the second experimental series is conducted with discs 7–12 of cylinder 1. The obtained data is displayed in Fig. 17. It immediately becomes apparent that there is no significant difference between the results of both microstructures. The variance in the measured signals is without any tendency towards either side, and the linear fits of both data sets are close to indistinguishable. Only the measurements at 1173 K show a slightly higher variation than the measurements before. This is attributed to the fact that with increasing temperature, the furnace of the LFA equipment had increasing trouble in keeping the temperature at a constant level, which affects the sensor in its performance. According to ASTM E 1461-01, the thermal diffusivity can be applied to the following Equation to determine the thermal conductivity:

$$k\ (T) = d\ (T)*c_p\ (T)*\rho\ (T) \tag{19}$$

3.8.3. Modeling of the thermal conductivity

Equation (19) is used to convert the experimental data, which is then included into the data set of experimental data from the literature. Finally, the whole data set is fitted in three sections corresponding to the phase composition. For $T_R < T <= T_\beta$, k is determined as

$$k_{\alpha'}\ (T) = 0.012\ [W/(mK)]\ *T/[K] + 3.3\ [W/(mK)] \tag{20}$$

The next section of $T_\beta < T <= T_l$ as well as $T_l < T$ yield

$$k_\beta\ (T) = 0.016\ [W/(mK)]\ *T/[K] - 3\ [W/(mK)] \tag{21}$$

$$k_l\ (T) = 0.0175\ [W/(mK)]\ *T/[K] - 4.5\ [W/(mK)] \tag{22}$$

The result of the fitting procedure is presented in Fig. 18. For the complete model including both heating and cooling of the material, Table 10 summarizes the respective temperature intervals according to Section 2 as well as the corresponding function.

3.9. Absorption

The heat input in PBF-LB/M is introduced by laser radiation, which is either reflected from, transmitted through or absorbed by the material. Only the absorbed radiation is heating the material. Therefore, this parameter has to be modeled as well. Little work has been done on the absorptivity of Ti–6Al–4V, though, as can be seen in Table 4. Nevertheless, some values have been determined experimentally, which are displayed in Fig. 19 and range from 0.34 to 0.55. Keller et al. [61] and Munsch [56] both found $a = 0.4$, Keller et al. later added a correction term to account for radiation losses, though. For the model of this study, the median $a = 0.4$ is considered. Yang et al. [57] have found that a is independent from T, so no further modeling is necessary.

3.10. Properties of the powder material

Since the material is introduced to the manufacturing process as powder, the thermal properties – namely ρ, c_p, and k – have to be modeled for powder material, too. Because ρ as well as c_p are material properties independent from the materials geometry, they can be related to the porosity ϕ:

$$P_p\ (T) = (1\text{-}\phi)*\rho(T) \tag{23}$$

$$c_{p,p}\ (T) = (1\text{-}\phi)*\ c_p\ (T) \tag{24}$$

For the thermal conductivity, this is not the case, though. The powder bed in PBF-LB/M consists of randomly packed particles, which can be assumed spherical and smooth [8,91]. Furthermore, the particles diameters are distributed over a certain interval, e.g. 20–63 µm. It can be classified as multiphase heterogeneous medium with the structure of a packed bed, with solid particles being dispersed in a continuous gas phase, touching each other though [92]. Depending on the powder application and the part already built, if investigated during the manufacturing process, the contact between the particles can be ideal point contacts or slightly elastically deformed contacts. While there is a long history in research regarding the thermal conductivity of packed

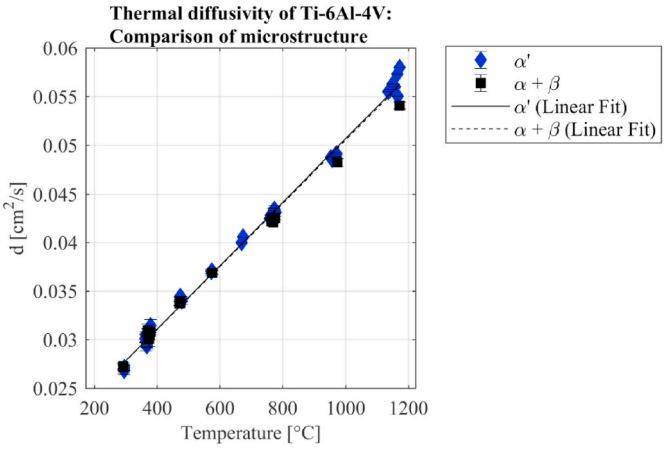

Fig. 17. Experimental results of LFA for comparison of α'- and (α+β)-microstructure.

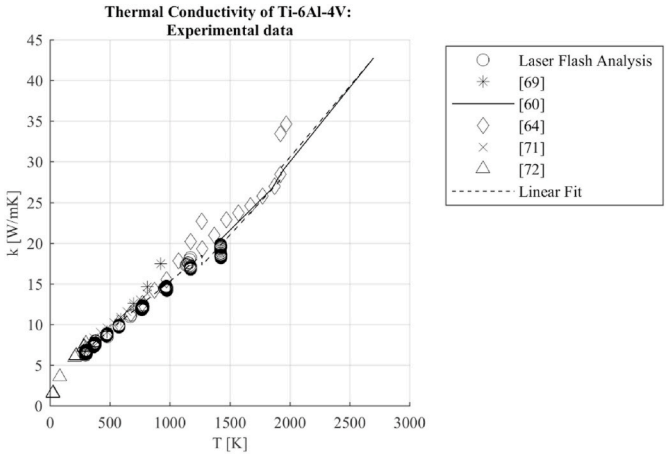

Fig. 18. Result of the fitting procedure for the modeling of the thermal conductivity.

Table 10
Material model of Ti–6Al–4V – Thermal conductivity, functions and temperature intervals for one full temperature cycle (upper section: heating, lower section: cooling).

Temperature	Microstructural phase	Function
$T_R < T <= T_\beta$	α'	$k_{\alpha'}(T)$
$T_\beta < T <= T_L$	β	$k_\beta(T)$
$T_L < T$	liquid	$k_l(T)$
$T_S < T$	liquid	$k_l(T)$
$T_{\alpha'S} < T <= T_S$	β	$k_\beta(T)$
$T_R < T <= T_{\alpha'S}$	α'	$k_{\alpha'}(T)$

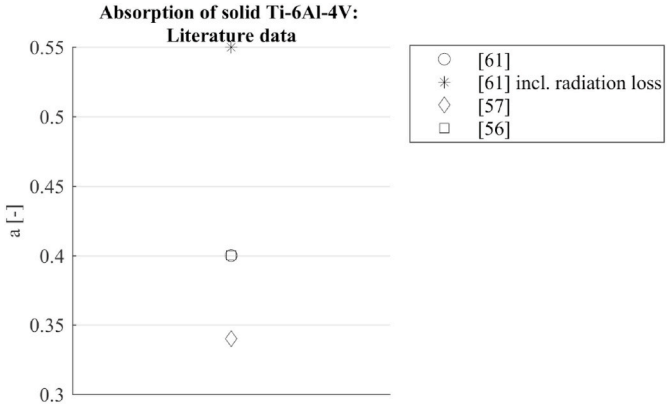

Fig. 19. Experimental data from the literature for the absorptivity.

beds, see De Beer et al. [93] for a comprehensive review, the case of the PBF-LB/M powder bed is still to be determined. Gusarov & Kovalev [92] derived a model based on the random packing of equally sized particles for the description of k in PBF-LB/M by modeling the discrete thermal resistance. Even though their calculations show the same tendencies, it underestimates the experimental data. They attribute this difference to the non-sphericity of the particles as well as the distribution in size, which is not included in their model. Gu et al. [91] determined the thermal conductivity of Ti–6Al–4V powder batches from several suppliers by scanning the powder bed in a PBF-LB/M manufacturing system until steady state conditions are met, and applied infra-red imaging to determine the changes in temperature. They do not mention whether process gas was used, and – if so – which gas. Consequently, the data cannot be included into the model of this study. However, they were able to demonstrate the importance of the powder batch characteristics: While two of three powder batches resulted in a powder thermal conductivity of 20% of the solid material's, the third powder batch exhibited a ratio of around 60%. This increase was attributed to agglomerated fine particles observed in the Scanning Electron Microscopy (SEM) images, highlighting the importance of controlled procedures in powder recycling. Recently, Wei et al. [94] investigated the thermal conductivity of powder beds made of Inconel 718, Inconel 625, Ti–6Al–4V, stainless steel 17-4, and stainless steel 316L via transient hot wire method. For Ti–6Al–4V under ambient pressure, the thermal conductivity ranges from appr. 0.2 W/(mK) at 300 K to 0.25 W/(mK) at 450 K, exhibiting a linear behavior. Because of the sparse data, an own powder sample taken directly from a PBF-LB/M system, therefore being in a mixed state of fresh and recycled powder, is commissioned to the Thermal Analysis Lab, Fredericton, Canada. Here, the thermal conductivity of the sample is investigated using a C-Therm TCi Thermal Conductivity Analyzer (C-Therm Technologies, Inc., Fredericton, Canada). The C-Therm TCi operates on a Modified Transient Plane Source sensor and in compliance with ASTM D7984-16. The powder is loaded in a high pressure liquids cell accessory, which was flushed with argon prior to the measurements. A weight of 75g was applied on top of the powder to slightly compact the powder poured into the sample holder for better contact to the heat source. Each value for a specific temperature is determined by calculating the mean of five consecutive measurements. The results are given in Fig. 20. At 373 K, a dip is noticed, which proved to be reproducible. An explanation lies within the fact that the powder sample consists of recycled powder and has been shipped from Germany to Canada, possibly leading to water accumulation. When heated up, the water evaporates at around 373 K. Part of the energy introduced into the experimental setup is used for the phase transformation instead of being conducted, resulting in a seemingly lower thermal conductivity. All in all, a linear relationship between T and k is found, which can be described as

$$k_P(T) = 327.6*10^{-6}\ [\mathrm{W/(mK)}]\ *T/[\mathrm{K}] + 0.079\ [\mathrm{W/(mK)}] \quad (25)$$

Finally, the powder absorptivity is determined by literature review. The small gaps between the powder particles trap the rays, because reflected rays may meet another powder particle, where again one part is reflected and another is absorbed. That way, the absorptivity of powder is significantly higher than for the solid material of the same alloy. This is also obvious when comparing the experimental data of solid (Fig. 19) and powder Ti–6Al–4V (Fig. 21), as processed in PBF-LB/M. The values found for powder absorptivity range from 0.65 to 0.74, while the solid absorptivity is determined to be in the interval of 0.34 to 0.55. Again, the median is considered for the model, yielding $a_p = 0.7$. Similar to a, Rubenchik et al. [54] found a_p to be independent of T.

4. Mechanical properties of Ti–6Al–4V

Because of the high strength to weight ratio of Ti–6Al–4V, the alloy is applied in industrial use cases with high loads or long operating times, as present in aerospace or medical industry. Therefore, the predictability of the mechanical properties of additively manufactured Ti–6Al–4V is considered a key challenge [95]. Consequently, a lot of research has been conducted towards this topic, summarized in Table 11. Note that studies providing their results as figures only have been excluded as the remaining data base is deemed sufficient. Typically, reports in literature show a higher strength of PBF-LB/M Ti–6Al–4V compared to conventionally processed specimens, as well as a lower ductility [95]. This is attributed to the finer microstructure as well as the presence of defects. Regarding the material properties necessary, two major issues arise, though: First, all data referenced in Table 11 has been acquired at room temperature, no experimental work on high temperature properties has been reported yet (to the author's best knowledge). Second, no data derived from specimens processed by PBF-LB/M has been found for the Poisson's ratio as well as the coefficient of thermal expansion. Even data on conventionally manufactured specimens is sparse. This lack of available data indicates a field of future research, and leads to the

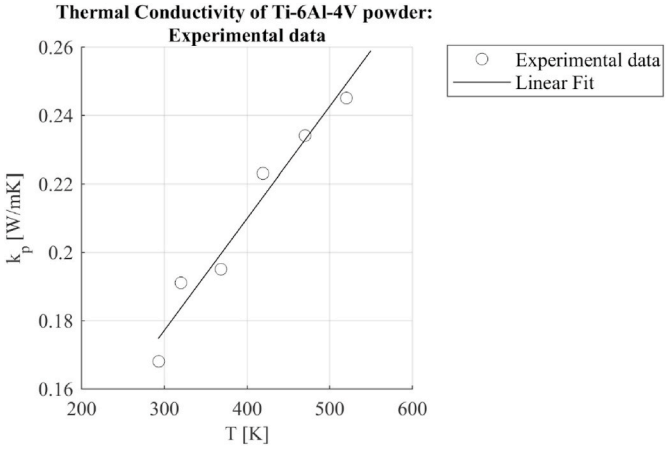

Fig. 20. Result of thermal conductivity measurements of the powder sample.

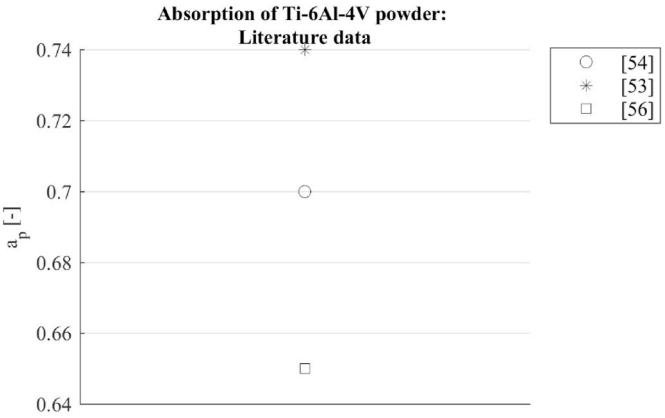

Fig. 21. Experimental data from the literature for the absorptivity of powder.

Table 11
Literature overview of tensile tests on PBF-LB/M Ti–6Al–4V specimen at room temperature (upper section) and experimental, temperature-dependent data for Poisson's ratio and CTE acquired by conventionally manufactured Ti–6Al–4V.

Source	as-built/ machined specimen	horizontal/vertical build orientation	*E*	σ_Y	*UTS*	ν	*CTE*
[106]	machined		x	x	x		
[107]	as-built	vertical	x	x			
[108]	as-built	horizontal	x	x	x		
[109]	as-built	vertical	x	x			
[110]	as-built	vertical			x		
[111]	as-built	horizontal, vertical	x	x	x		
[112]	machined			x	x		
[113]	machined	horizontal, vertical	x	x	x		
[114]	machined		x[a]		x[a]		
[115]	machined	vertical		x			
[116]	as-built	vertical	x	x	x		
[117]	machined	vertical	x	x	x		
[118]	as-built	horizontal, vertical	x	x	x		
[119]	machined	vertical		x	x		
[120]	machined	horizontal, vertical		x	x		
[121]	machined	vertical	x	x	x		
[104]	as-built, machined	vertical	x	x	x		
[122]	machined	horizontal	x	x	x		
[123]	machined	horizontal, vertical	x[a]	x[a]	x[a]		
[102]	as-built	horizontal		x	x		
[91]	machined	horizontal		x	x		
[124]	machined	vertical			x		
[97]	as-built	horizontal		x	x		
[98]	machined	horizontal, vertical	x	x	x		
[125]	machined		x	x	x		
[126]	as-built	vertical		x	x		
[127]	machined	horizontal, vertical		x	x		
[128]	as-built	vertical			x		
[129]	machined	horizontal	x	x	x		
[130]	as-built	horizontal, vertical	x	x	x		
[131]	as-built	horizontal	x	x	x		
[132]	as-built		x	x	x		
[133]	machined	horizontal	x	x	x		
[134]							x
[135]				x			
[136]				x	x		
[58]							x
[137]				x			
[138]				x	x	x	

[a] Data published as figure, raw data provided by authors upon request.

remark to use the model presented in this work with caution.

While there is a standard procedure to determine the monotonic tensile properties described in the ASTM E8 standard, there are still various influencing factors which have to be considered. The main influencing factor is the microstructure [96], whose anisotropy seems to affect the mechanical properties, as observed in the studies by Mertens et al. [97], Simonelli et al. [98], and Qiu et al. [99]. The scan strategy as well as the build orientation of the specimens are attributed a significant contribution to the anisotropy found in the microstructure of PBF-LB/M Ti–6Al–4V [100]. The difference in grain size with regard to the build orientation and perpendicular to it, as shown by Thijs et al. [101], should influence the yield strength according to the Hall-Petch law of grain boundary strengthening. Edwards & Ramulu [102] point out that this anisotropy is not always observed in experimental studies, though. Whereas the scan strategy is seldom described in publications, the build orientation is specified with little exceptions due to its known importance. Therefore, the anisotropy in the microstructure of the specimen due to the build orientation is examined to ensure that only representative data with respect to the system under consideration in this work is included. The terminology to exactly describe the build orientation is given in the ASTM/ISO 52921 standard, distinguishing between six different orientations of specimen for mechanical testing. The standard terminology has been developed throughout the last couple of years, though, and is not broadly applied in scientific publications yet. As a consequence, Table 11 only indicates whether the specimens have been built with the main axis in build direction (vertical orientation) or in the build plane (horizontal orientation).

In terms of chemical composition, the oxidation of the highly reactive Ti–6Al–4V alloy is known to have a high impact on the material performance [8–10]. The chemical composition of the specimens after manufacturing is rarely determined because of the effort and cost linked to the required techniques, hindering the systematic evaluation of this aspect to date. The influence of the oxygen content is thus not part of this work, but definitely requires attention in future studies. There are other influencing factors besides the microstructure of the specimen that can be taken into consideration, though. Specimens can have various geometries [103]: The test coupons can be flat or cylindrical, and the compact tensile specimens consist of a block with a notch. Furthermore, the surface roughness of PBF-LB/M specimens is higher than conventional specimens because of the powder involved in the processing [96], and Kasperovich & Hausmann [104] found in their study, that tensile specimens with machined surfaces exhibited greater strength than as-built specimens. They concluded that the surface roughness is a nucleus for crack initiation, as has been noticed in fatigue testing as well (see e.g. Ref. [105]). Again, to ensure the inclusion of representative data only, the influence of the surface condition is examined in this work. Table 11 indicates the surface conditions. Note that hybrid conditions, i.e. partially machined specimens as produced when removing support structures from one side, are considered "machined". If no post-processing of the specimens is mentioned, the specimens are assumed to be tested "as-built".

Additional post-processing techniques, especially heat treatments, do have a major influence on the microstructure and thus the mechanical properties. Since the focus of the work is on the modelling of the manufacturing, though, any data on heat-treated tensile specimens is excluded. Interested readers are hereby referred to the reviews of Agius et al. [103], Beese & Carroll [95], Lewandowski et al. [100], and Tong et al. [96] for a broad overview of literature regarding the tensile properties of heat-treated PBF-LB/M Ti–6Al–4V specimens.

Because of the amount of influencing factors to the mechanical properties of Ti–6Al–4V, no own experimental work is conducted as no substantial insights are expected to be gained. Instead, the experimental data from the literature is used to find the respective values of E and σ_Y at room temperature. Additionally, the value for *UTS* is determined to assist in the interpretation of simulation results. E and σ_Y are then fitted, using data of conventional Ti–6Al–4V (see Table 11) as well as material models of published computational works as orientation for the parameter development over temperature. ν and *CTE* are determined with the works shown in Table 11.

Prior to the modeling procedure, the tensile data is evaluated in terms of the following suspected influences: surface condition, build

orientation, and date of the publication, as the rapid innovation of manufacturing systems in the field of PBF-LB/M may result in significant differences in microstructure depending on the time of manufacturing. The data for E is displayed in Fig. 22 and Fig. 23. Because the surface condition is relevant regarding crack initiation, there is no influence of the surface condition on E to be evaluated.

In Fig. 22, the data is categorized by the build orientation. Additionally, if a publication evaluated both orientations, those data pairs are indicated by a connecting lines. This data is especially interesting, since the specimens have been manufactured under the same conditions. Of five data pairs, three show a higher Young's modulus for the vertical build orientation, whereas two data pairs present the opposite. The maximum deviation in E between the orientations is presented by Mower & Long [118] with 108.8 GPa for the horizontal and 114.9 GPa for the vertical build orientation, yielding a difference of 5.6%. Also, no clear difference between the two build orientations is observed in general: The median of the Young's modulus of the horizontal build orientation data set is $E_{hor,med} = 109$ GPa, the median of the other data set is $E_{ver,med} = 110$ GPa.

With regard to the last evaluated influencing factor, Fig. 23 displays the experimental data of Table 11 with respect to the year of publication. The time ranges from 2006 to 2020, and an increasing number of publications since 2014 is observed. Nonetheless, both the earliest publications of Hollander et al. [133] and Vandenbroucke & Kruth [132] exhibit a similar range in E as the latest publications do.

The same comparison of data is carried out for σ_Y, shown in Fig. 24, Fig. 25, and Fig. 26. Overall, the same observations as for E are made. The range of the data sets categorized by surface condition (Fig. 24) show a similar range of values, and the median of the data sets are $\sigma_{Y,machined,med} = 1095.5$ MPa, and $\sigma_{Y,as\text{-}built,med} = 1027.3$ MPa. As the standard deviations are 100.9 MPa and 116.7 MPa, respectively, no significance is attributed. The suspected anisotropy due to the build orientation, see Fig. 25, is not clearly identified, also. Five data pairs show higher strength for the horizontal build orientation, while two data pairs demonstrate the opposite. The corresponding median yield stress is $\sigma_{Y,hor,med} = 1100$ MPa and $\sigma_{Y,ver,med} = 1064.8$ MPa, respectively. Compared to the data evaluated for E, though, the deviations of the related data are larger. The maximum difference in a single experimental study is shown by Vilaro et al. [130] with a yield strength of 1137 MPa for the horizontal and 962 MPa for the vertical build orientation, resulting in an 18.1% deviation, which is considered significant. Another interesting observation to point out are the studies of Mower & Long [118] and Cain et al. [120]: Both found a yield strength of 1096 MPa or 1093 MPa for the vertical build orientation, respectively. Their values for the horizontal build orientation differ by 15.7% (972 MPa/1125 MPa), though, and do not match in the overall tendency of the development in regard to the vertical build orientation. Finally, the chronological development of the experimental data does not indicate any relation of the data to the year of publication.

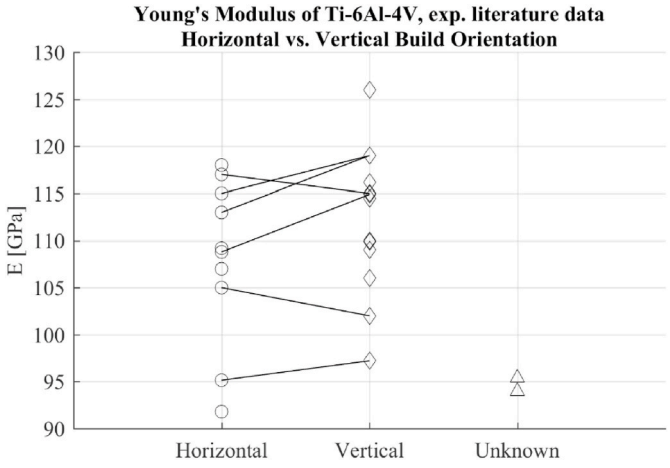

Fig. 22. Experimental data on the Young's modulus of PBF-LB/M Ti–6Al–4V, according to Table 11, categorized by build orientation of the specimen.

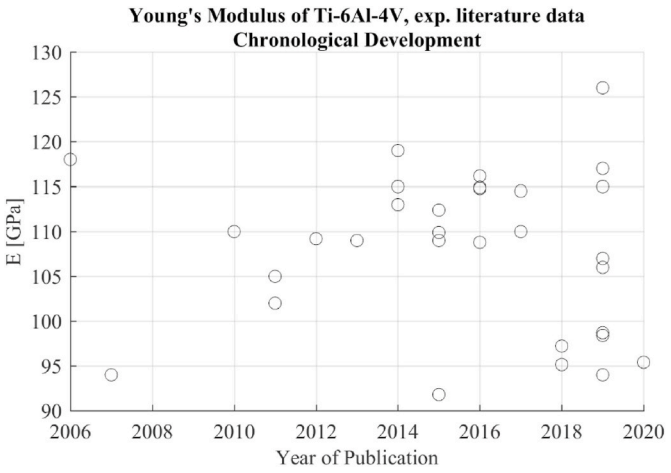

Fig. 23. Experimental data on the Young's modulus of PBF-LB/M Ti–6Al–4V, according to Table 11, sorted by the year of publication.

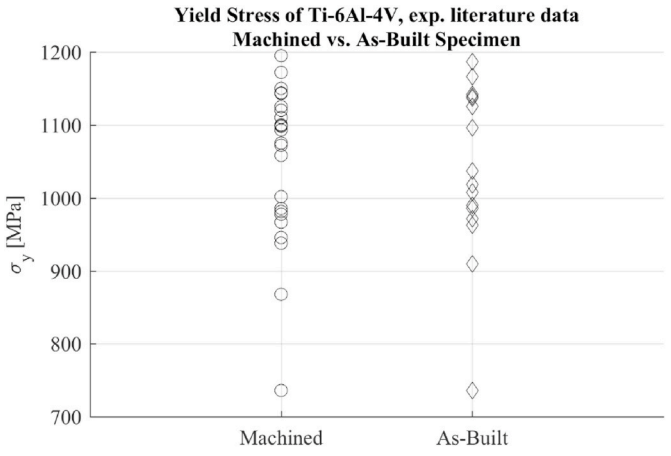

Fig. 24. Experimental data on the yield stress of PBF-LB/M Ti–6Al–4V, according to Table 11, categorized by surface condition.

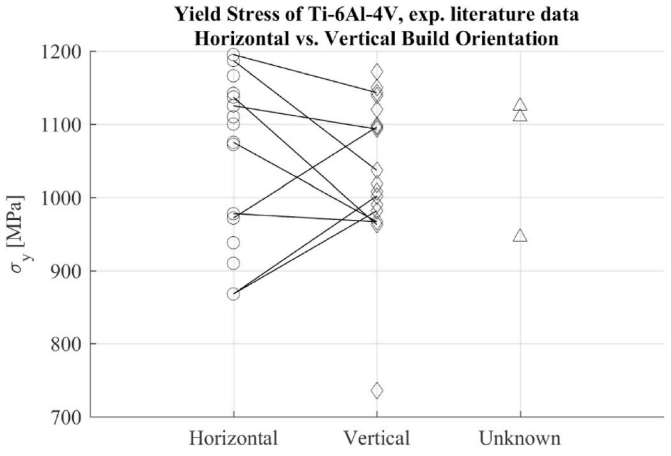

Fig. 25. Experimental data on the yield stress of PBF-LB/M Ti–6Al–4V, according to Table 11, categorized by build orientation.

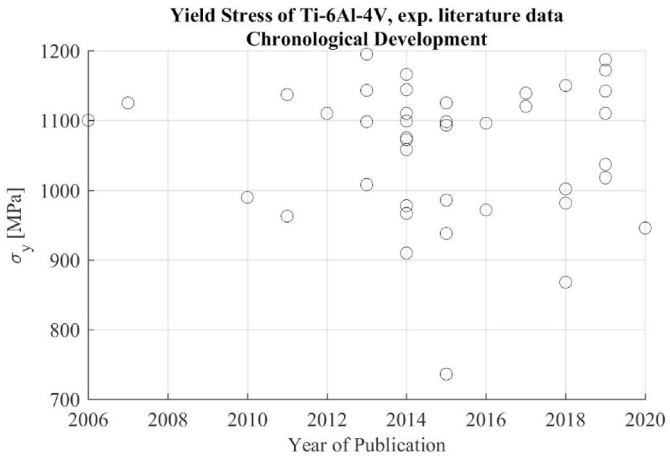

Fig. 26. Experimental data on the yield stress of PBF-LB/M Ti–6Al–4V, sorted by the year of publication.

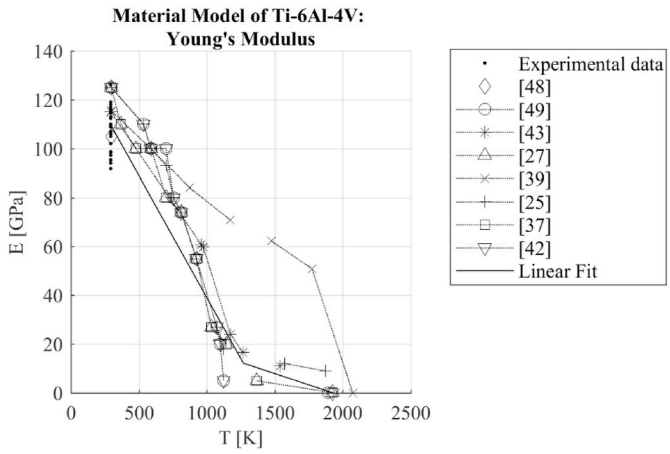

Fig. 27. Result of the fitting procedure for the modeling of the Young's modulus.

In conclusion, the data evaluated does not show a direct anisotropy in the Young's modulus or yield strength related to either surface condition, build orientation, or chronological sequence. For σ_y evaluated in terms of build orientation there are significant differences in related data sets, but no specific relationship can be derived. This indicates that there may be anisotropy which is superimposed by other factors influencing the mechanical properties, such as residual stresses [103]. Further effort in research is necessary to clarify the key factors to mechanical anisotropy and the influence of process parameter on the individual factors, which is not within the scope of this study. Also, depending on the process parameters applied, anisotropy will develop different, similar to the microstructure. As this material model is not meant to be tailored to a specific manufacturing system and set of process parameters, all references presented are included into the modeling of the mechanical material properties. In consequence, the following mechanical material model does not consider further microstructural properties, e.g. grain boundaries, orientation, and size, but aims to develop a generic description of the mechanical behavior of Ti–6Al–4V.

4.1. Young's modulus of Ti–6Al–4V

For the modeling of E, the different intervals of microstructural composition of the solid material (α', β, liquid) are considered. First, the value at room temperature ($T_R = 293$K) is determined by calculating the median of all experimental data presented in Table 11, $E_{med} = 109.1$ GPa. As for the linear fitting a second data point is required, but no experimental data on PBF-LB/M Ti–6Al–4V at other temperatures is available, the material models of published computational works are used as an indicator. As most of the material models are either not referenced or referenced to another simulation, the data is not directly included into the fitting procedure. Fig. 27 displays the references as well as their applied data taken into account. Note that studies which give their model as figures only have been excluded. It is concluded, that the Young's modulus at T_β has a value of ca. 10 GPa, the study of Mukherjee et al. [25] being the only exception. This leads to the following linear function:

$$E_{\alpha'} = \text{-0.102 [GPa] } *T/\text{[K]} + 139 \text{ [GPa]} \quad (25)$$

When the material is molten, the Young's modulus is nonexistent. Since an assigned value of "0" can lead to singularities in computation, E is set to 10^{-9} GPa at T_L. Accordingly, the linear function for the interval of β phase microstructure is:

$$E_\beta = \text{-0.0145 [GPa] } *T/\text{[K]} + 28 \text{ [GPa]} \quad (26)$$

Note that Function 26 had to be slightly adjusted, because the rounding errors of Function 25 set the function's value at T_β to 9.664 GPa instead of 10 GPa. In the liquid phase, E is assumed constant:

$$E_L = 10^{-9} \text{ [GPa]} \quad (27)$$

The result of the fit is presented in Fig. 27. To give a complete material model including both heating and cooling of the material, Table 12 summarizes the respective temperature intervals according to Section 2 as well as the corresponding function.

4.2. Yield stress of Ti–6Al–4V

For the modeling of σ_Y, a similar procedure as for E is applied. The median of the experimental data displayed in Table 11 yields $\sigma_{Y,med} = 1094.5$ MPa at room temperature. Fig. 28 shows the experimental data as well as the data used in published computational work. Besides the models applied in the studies of Mukherjee et al. [25] and Xiao et al. [42], the material models suggest a linear behavior, which is supported by the experimental data on conventionally processed Ti–6Al–4V of Table 11. At T_β most of the models agree on σ_Y approaching a value of approx. 5 MPa. Equal to E, σ_Y is taken as close to zero. Therefore, the functions describing the yield stress are:

$$\sigma_{Y,\alpha'} = \text{-1.117 [MPa] } *T/\text{[K]} + 1422.6 \text{ [MPa]} \quad (28)$$

$$\sigma_{Y,\beta} = \text{-9.46*}10^{-3} \text{ [MPa] } *T/\text{[K]} + 18.2 \text{ [MPa]} \quad (29)$$

$$\sigma_{Y,L} = 10^{-6} \text{ [MPa]} \quad (30)$$

Again, function 29 is slightly adjusted to the rounding errors of function 28, which yields a value of 6.244 MPa at T_β. The result of the fitting procedure is presented in Fig. 28 also. For the complete material model, the sequence for one full cycle of heating and cooling is given in Table 13.

Table 12
Material model of Ti–6Al–4V – Young's modulus, functions and temperature intervals for one full temperature cycle (upper section: heating, lower section: cooling).

Temperature	Microstructural phase	Function
$T_R < T <= T_\beta$	α'	$E_{\alpha'}$
$T_\beta < T <= T_L$	β	E_β
$T_L < T$	liquid	E_L
$T_S < T$	liquid	E_L
$T_{\alpha'S} < T <= T_S$	β	E_β
$T_R < T <= T_{\alpha'S}$	α'	$E_{\alpha'}$

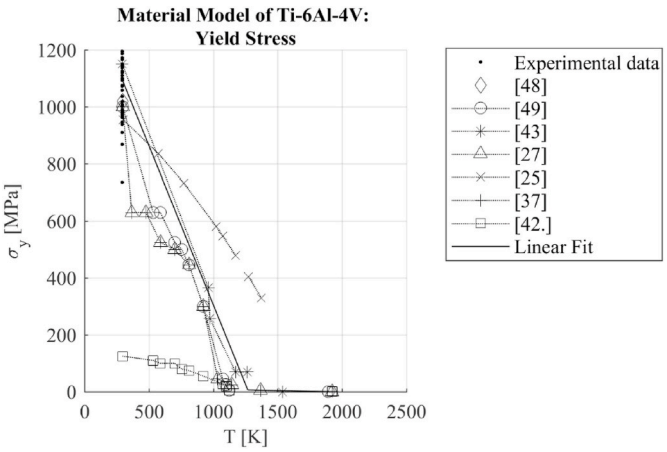

Fig. 28. Result of the fitting procedure for the modeling of the yield stress.

Table 13
Material model of Ti–6Al–4V – yield stress, functions and temperature intervals for one full temperature cycle (upper section: heating, lower section: cooling).

Temperature	Microstructural phase	Function
$T_R < T <= T_\beta$	α'	$\sigma_{Y,\alpha'}$
$T_\beta < T <= T_L$	β	$\sigma_{Y,\beta}$
$T_L < T$	liquid	$\sigma_{Y,L}$
$T_S < T$	liquid	$\sigma_{Y,L}$
$T_{\alpha'S} < T <= T_S$	β	$\sigma_{Y,\beta}$
$T_R < T <= T_{\alpha'S}$	α'	$\sigma_{Y,\alpha'}$

4.3. Ultimate tensile strength of Ti–6Al–4V

The *UTS* is usually not modeled in process simulation, as most commercial software does support mesh deformation, but no mesh splitting as would be necessary to exactly model the fracture of material. It is important, though, to be aware of the *UTS* to interpret computational results correctly. Thus, *UTS* is not fully modeled here, but the median of the experimental data is given: $UTS_{med} = 1202.5$ MPa for T_R. For increasing temperature, the data of Sieniawski et al. [136] and Lütjering [138] indicate linear behavior as seen in σ_Y.

4.4. Poisson's ratio of Ti–6Al–4V

Experimental data on ν of PBF-LB/M Ti–6Al–4V is not available within the studies evaluated in Table 11, and only one reference [138] has been found on conventionally processed material. Without the option of own experimental work, data from published computational studies has to be used as well, presented in Fig. 29. As can be seen, Chen et al. [49] and Xiao et al. [42] both reference the same computational study of Ragaswamy et al. [46], where no further reference or explanation of the origin of the data is given. The experimental data of Lütjering [138] is lower in terms of actual values, but exhibits a steeper slope in the development over temperature. No change in the slope of the data is noticed above T_β, which may be due to the lack of data. Nonetheless, based on the data presented in Fig. 29, the function for ν in the solid state is determined as:

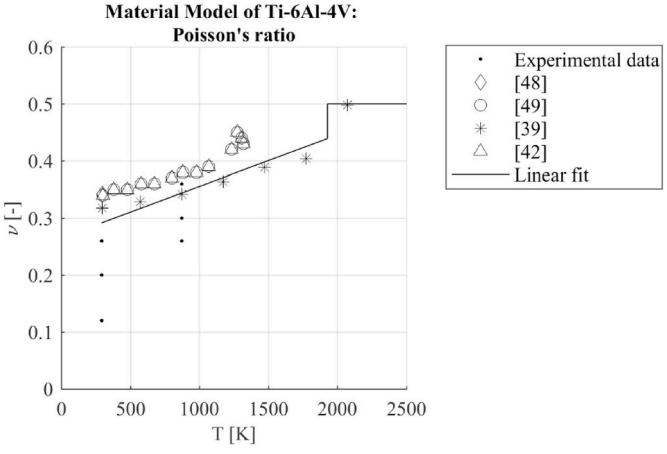

Fig. 29. Result of the fitting procedure for the modeling of the Poisson's ratio.

$$\nu_{\alpha',\beta} = 9*10^{-5}*T/[\mathrm{K}] + 0.2655 \quad (31)$$

At T_R, Function 31 yields a value of 0.29, which is well within the known range of ν (0.25 .. 0.4; see e.g. Ref. [139]) for titanium alloys. In the liquid state, the molten material expands or contracts isotropically, resulting in a constant value:

$$\nu_L = 0.5 \quad (32)$$

The modeling sequence for a full cycle of heating and cooling is summarized in Table 14.

4.5. Coefficient of thermal expansion of Ti–6Al–4V

As the parameter that links thermal and mechanical physics, the *CTE* is of high importance for the thermo-mechanical process simulation. Still, similar to ν, there is no data within the evaluated references for PBF-LB/M Ti–6Al–4V. Therefore, other experimental values as well as process simulation studies are used for fitting. The following description of the *CVTE* is determined:

$$CTE_{\alpha'} = 0.004197\ [1/\mathrm{K}]\ *T/[\mathrm{K}] + 7.758\ [1/\mathrm{K}] \quad (33)$$

$$CTE_{\beta} = 0.00051\ [1/\mathrm{K}]\ *T/[\mathrm{K}] + 12.427\ [1/\mathrm{K}] \quad (34)$$

$$CTE_L = 20.71\ [1/\mathrm{K}] \quad (35)$$

Since no data is available for liquid metal in higher temperature intervals, the CTE_L is modeled as constant. In PBF-LB/M, since the liquid metal represents the upper layer, there is no possibility of load transfer or creating distortion within the liquid metal, therefore the nature of the *CTE* is not relevant. The result of the fitting is shown in Fig. 30, together with experimental data as denoted in Table 11 and material models from other computational works. Note that the data points from Li [58] are experimental values from conventionally processed Ti–6Al–4V also, but since Li determined the *CVTE*, the data points have been converted to *CTE* by means of Equation (6). The modeling sequence for a complete cycle of heating and cooling is given in Table 15.

5. Conclusion

The computational modeling of additive manufacturing processes is essential to increase the technologies' maturity while reducing the required resources to a reasonable amount. Beside the on-going research to develop approaches capable of dealing with the problem of dimensional scales especially in laser additive manufacturing, the modeling of

Table 14
Material model of Ti–6Al–4V – Poisson's ratio, functions and temperature intervals for one full temperature cycle (upper section: heating, lower section: cooling).

Temperature	Microstructural phase	Function
$T_R < T <= T_\beta$	α'	$\nu_{\alpha',\beta}$
$T_\beta < T <= T_L$	β	$\nu_{\alpha',\beta}$
$T_L < T$	liquid	ν_L
$T_S < T$	liquid	ν_L
$T_{\alpha'S} < T <= T_S$	β	$\nu_{\alpha',\beta}$
$T_R < T <= T_{\alpha'S}$	α'	$\nu_{\alpha',\beta}$

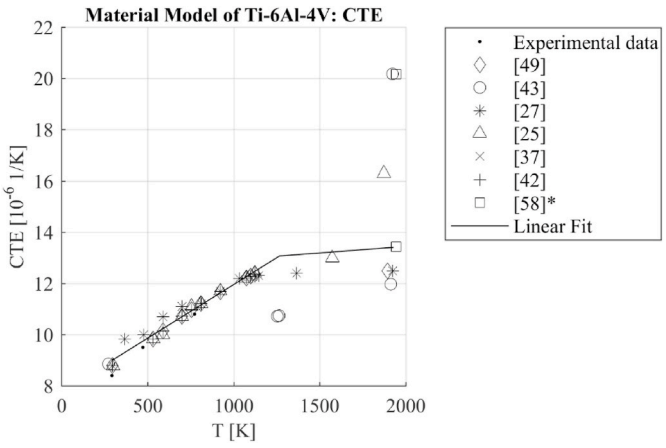

Fig. 30. Result of modeling procedure for the coefficient of thermal expansion (*data converted from CVTE to CLTE).

Table 15
Material model of Ti–6Al–4V – coefficient of thermal expansion, functions and temperature intervals for one full temperature cycle (upper section: heating, lower section: cooling).

Temperature	Microstructural phase	Function
$T_R < T <= T_\beta$	α'	$CTE_{\alpha'}$
$T_\beta < T <= T_L$	β	CTE_β
$T_L < T$	liquid	CTE_L
$T_S < T$	liquid	CTE_L
$T_{\alpha'S} < T <= T_S$	β	CTE_β
$T_R < T <= T_{\alpha'S}$	α'	$CTE_{\alpha'}$

the applied materials offers the possibility to increase the accuracy of process simulation with no significant increase of the required computational resources. Yet there exist no standardized material models even for the common materials used. This study has taken the first step towards the development of a material model for the thermo-mechanical process simulation of PBF-LB/M at macro- and part-scale. Data from the literature has been gathered, examined and processed to a material model consisting of either constant values or step-wise linear functions. Furthermore, the thermal properties of the martensitic material produced by PBF-LB/M have been compared to those of the common (α+β)-microstructure achieved by conventional manufacturing. No significant difference has been found. Additionally, the available data on mechanical material properties have been investigated to identify possible influences due to the build orientation of specimens, the surface condition of specimens, and the advancement of the technology over time. Again, no significant influence in the surface condition and the chronological sequence has been detected. For the yield strength, some datasets evaluated indicate a relationship of anisotropic yield strength and the build orientation. A quantification of this relationship was not possible, though.

One major challenge in this study has been the availability of data. Especially at higher temperatures, the data reported in the literature is sparse. Furthermore, the results of experimental studies are often presented as figures only, and sometimes are not available anymore after some years as the responsible authors have left the institution. This hinders the process of collaborative material modeling, emphasizing the importance of publishing the raw data in data repositories and the development of collaborative databases. The experimental data of the DSC as well as LFA for the supplement of the data on the thermal properties of Ti–6Al–4V is published in the data repository of Hamburg University of Technology [140].

The second challenge that has become obvious in this study is the variance in reported experimental data and the existence of unquantified, even unknown influencing factors besides the temperature, respectively. The linear functions chosen to approximate the data do not always exactly fit the tendencies of those. To be able to fit the data with functions of higher order, it is necessary to be able to identify the additional influences, though. Especially the influence of the oxygen content is highly relevant here. This requires further research on the one hand, and the consequent reporting of all known influencing factors when publishing experimental studies on the other hand. Standardized protocols not only for the procedures, but also for the reports, with respect to the individual measuring methods would be of high benefit towards a global effort for the complete characterization of materials.

Funding

This research did not receive any specific grant from funding agencies in the public, commercial, or not-for-profit sectors.

Data availability

The raw and processed data required to reproduce these findings are available to download from Ref. [132].

CRediT authorship contribution statement

Katharina Bartsch: Conceptualization, Methodology, Investigation, Writing – original draft. **Dirk Herzog:** Conceptualization, Methodology, Writing – review & editing. **Bastian Bossen:** Methodology, Writing – review & editing. **Claus Emmelmann:** Conceptualization.

Declaration of competing interest

The authors declare that they have no known competing financial interests or personal relationships that could have appeared to influence the work reported in this paper.

Acknowledgements

The authors would like to thank Dr. Thomas Ebel and Martin Wolff from Helmholtz Zentrum Geesthacht – Center for Materials and Coastal Research for the possibility of and support in the Differential Scanning Calorimetry Experiments. Further thanks goes to Prof. Dr.-Ing. Manfred Eich, Dr. rer. nat. Alexander Petrov, and Dr. Guoliang Shang of the Institute of Optical and Electronic Materials (OEM) of Hamburg University of Technology, Germany, for providing access and an introduction to their Laser Flash Analysis equipment. Last, the authors would like to thank Sarah Ackermann from Thermal Analysis Lab for her giving valuable insights in the thermal analysis of materials.

References

[1] M.K. Thompson, G. Moroni, T. Vaneker, G. Fadel, R.I. Campbell, I. Gibson, A. Bernard, J. Schulz, P. Graf, B. Ahuja, F. Martina, Design for additive manufacturing: trends, opportunities, considerations, and constraints, CIRP Ann. - Manuf. Technol. 65 (2016) 737–760, https://doi.org/10.1016/j.cirp.2016.05.004.
[2] A.J. Pinkerton, Laser in additive manufacturing, Opt Laser. Technol. 78 (2016) 25–32, https://doi.org/10.1016/j.optlastec.2015.09.025.
[3] M.M. Francois, A. Sun, W.E. King, N.J. Henson, D. Tourret, C.A. Bronkhorst, N. N. Carlson, C.K. Newman, T. Haut, J. Bakosi, J.W. Gibbs, V. Livescu, S.A. Vander Wiel, A.J. Clarke, M.W. Schraad, T. Blacker, H. Lim, T. Rodgers, S. Owen, F. Abdeljawad, J. Madison, A.T. Anderson, J.-L. Fattebert, R.M. Ferencz, N. E. Hodge, S.A. Khairallah, O. Walton, Modeling of additive manufacturing processes for metals: challenges and opportunities, Curr. Opin. Solid State Mater. Sci. 21 (4) (2017) 198–206, https://doi.org/10.1016/j.cossms.2016.12.001.
[4] B. Dutta, F.H. Froes, The additive manufacturing (AM) of titanium alloys, in: M. Qian, F.H. Froes (Eds.), Titanium Powder Metallurgy, Butterworth-Heinemann, 2015, pp. 447–468, https://doi.org/10.1016/B978-0-12-800054-0.00024-1.
[5] W.S.W. Harun, M.S.I.N. Kamariah, N. Muhamad, S.A.C. Ghani, F. Ahmad, Z. Mohamed, A review of powder additive manufacturing processes for metallic

biomaterials, Powder Technol. 327 (2018) 128–151, https://doi.org/10.1016/j.powtec.2017.12.058.
[6] O. Quénard, O. Dorival, P. Guy, K. Brethome, MEASUREMENT OF RESIDUAL STRESSES AND TOUGHNESS IN Ti-6Al-4V MATERIAL PRODUCED BY LASER BEAM MANUFACTURING, MATEC Web of Conferences 167 (2018), 02002, https://doi.org/10.1051/matecconf/201816702002.
[7] C. Li, Z.Y. Liu, X.Y. Fang, Y.B. Guo, Residual stress in metal additive manufacturing, Procedia CIRP 71 (2018) 348–353, https://doi.org/10.1016/j.procir.2018.05.039.
[8] V. Seyda, D. Herzog, C. Emmelmann, Relationship between powder characteristics and part properties in laser beam melting of Ti-6Al-4V, and implications on quality, J. Laser Appl. 29 (2017), 022311, https://doi.org/10.2351/1.4983240.
[9] M. Peters, J. Hemptenmacher, J. Kumpfert, C. Leyens, Structure and properties of titanium and titanium alloys, in: C. Leyens, M. Peters (Eds.), Titanium and Titanium Alloys, Wiley-VCH, Weinheim, Germany, 2003, pp. 1–36.
[10] G. Lütjering, J.C. Williams, Titanium, second ed., Springer-Verlag, Berlin Heidelberg New York, 2003, pp. 203–258.
[11] R. Stolt, F. Elgh, Introducing design for selective laser melting in aerospace industry, J. Comput.Des.Eng. 7 (2020) 1–9, https://doi.org/10.1093/jcde/qwaa042.
[12] C. Seidel, M.F. Zaeh, M. Wunderer, J. Weirather, T.A. Krol, M. Ott, Simulation of the laser beam melting process – approaches for an efficient modelling of the beam-material interaction, Procedia CIRP 25 (2014) 146–153, https://doi.org/10.1016/j.procir.2014.10.023.
[13] M. Chiumenti, E. Neiva, E. Salsi, M. Cervera, S. Badia, J. Moya, Z. Chen, C. Lee, C. Davies, Numerical modelling and experimental validation in selective laser melting, Addit. Manuf. 18 (2017) 171–185, https://doi.org/10.1016/j.addma.2017.09.002.
[14] W. Kritzinger, M. Karner, G. Traar, J. Henjes, W. Sihn, Digital Twin in manufacturing: a categorical literature review and classification, IFAC PapersOnLine 51 (11) (2018) 1016–1022, https://doi.org/10.1016/j.ifacol.2018.08.474.
[15] W. King, A.T. Anderson, R.M. Ferencz, N.E. Hodge, C. Kamath, S.A. Khairallah, Overview of modelling and simulation of metal powder bed fusion process at Lawrence Livermore National Laboratory, Mater. Sci. Technol. 31 (8) (2015) 957–968, https://doi.org/10.1179/1743284714Y.0000000728.
[16] Y. Chen, H. Chen, J. Chen, J. Xiong, Y. Wu, S. Dong, Numerical and experimental investigation on thermal behavior and microstructure during selective laser melting of high strength steel, J. Manuf. Process. 57 (2020) 533–542, https://doi.org/10.1016/j.jmapro.2020.06.041.
[17] L. Zhang, K. Wu, Q. Yang, X. Ni, T. Wang, W. Wu, L. Lu, Effect of heat input parameters on molten pool size during selective laser melting of Ti-6Al-4V powder through numerical simulation, IOP Conf. Ser. Mater. Sci. Eng. 730 (2020), 012003, https://doi.org/10.1088/1757-899X/730/1/012003.
[18] M. Majeed, H.M. Khan, I. Rasheed, Finite element analysis of melt pool thermal characteristics with passing laser in SLM process, Optik 194 (2019) 163068, https://doi.org/10.1016/j.ijleo.2019.163068.
[19] Q. Zhang, J. Xie, Z. Gao, T. London, D. Griffiths, V. Oancea, A metallurgical phase transformation framework applied to SLM additive manufacturing processes, Mater. Des. 166 (2019) 107618, https://doi.org/10.1016/j.matdes.2019.107618.
[20] Z. Wang, M. Liu, Dimensionless analysis on selective laser melting to predict porosity and track morphology, J. Mater. Process. Technol. 273 (2019) 116238, https://doi.org/10.1016/j.jmatprotec.2019.05.019.
[21] E. Mirkoohi, D.E. Sievers, H. Garmestani, S.Y. Liang, Heat source modeling in selective laser melting, Materials 12 (2019) 2052, https://doi.org/10.3390/ma12132052.
[22] A.K. Mishra, A. Kumar, Numerical and experimental analysis of the effect of volumetric energy absorption in powder layer on thermal-fluidic transport in selective laser melting of Ti-6Al-4V, Opt Laser. Technol. 111 (2019) 227–239, https://doi.org/10.1016/j.optlastec.2018.09.054.
[23] E. Soylemez, High deposition rate approach of selective laser melting through defocused single bead experiments and thermal finite element analysis for Ti-6Al-4V, Addit. Manuf. 31 (2019) 100984, https://doi.org/10.1016/j.addma.2019.100984.
[24] X. Xing, Q. Zhou, S. Wang, L. Wang, F. Jiang, Numerical investigation of transient temperature distribution during Ti-6Al-4V selective laser melting, J. Therm. Sci. 28 (2019) 370–377, https://doi.org/10.1007/s11630-019-1082-z.
[25] T. Mukherjee, W. Zhang, T. DebRoy, An improved prediction of residual stresses and distortion in additive manufacturing, Comput. Mater. Sci. 126 (2017) 360–372, https://doi.org/10.1016/j.commatsci.2016.10.003.
[26] M.S. Rahman, P.J. Schilling, P.D. Herrington, U.K. Chakravarty, A comparative study between selective laser melting and electron beam additive manufacturing based on thermal modeling, in: Proceedings of the ASME 2018 International Mechanical Engineering Congress and Exposition, 2019, https://doi.org/10.1115/IMECE2018-86428. V001T03A015.
[27] S. Saxena, R. Sharma, A. Kumar, A microscale study of thermal field and stresses during processing of Ti-6Al-4V powder layer by selective laser melting, Laser. Manuf.Mater.Process 5 (4) (2018) 335–365, https://doi.org/10.1007/s40516-018-0070-6.
[28] C. Panwisawas, C. Qiu, M.J. Anderson, Y. Sovani, R.P. Turner, M.M. Attallah, J. W. Brooks, H.C. Basoalto, Mesoscale modelling of selective laser melting: thermal fluid dynamics and microstructural evolution, Comput. Mater. Sci. 126 (2017) 479–490, https://doi.org/10.1016/j.commatsci.2016.10.011.
[29] J. Romano, L. Ladani, M. Sadowski, Thermal modeling of laser based additive manufacturing processes within common materials, Procedia Manufacturing 1 (2015) 238–250, https://doi.org/10.1016/j.promfg.2015.09.012.
[30] C.H. Fu, Y.B. Guo, 3-dimensional finite element modeling of selective laser melting Ti-6Al-4V alloy, in: Proceedings of the 25th Annual International Solid Freeform Fabrication Symposium, 2014, pp. 1129–1144. Texas, USA.
[31] Z. Fan, F. Liou, Numerical modeling of the additive manufacturing (AM) processes of titanium alloy, in: A.K.M. Nurul Amin (Ed.), Titanium Alloys: towards Achieving Enhanced Properties for Diversified Applications, 2012, pp. 3–28.
[32] C. Körner, E. Attar, P. Heinl, Mesoscopic simulation of selective beam melting processes, J. Mater. Process. Technol. 211 (2011) 978–987, https://doi.org/10.1016/j.jmatprotec.2010.12.016.
[33] F. Verhaeghe, T. Craeghs, J. Heulens, L. Pandelaers, A pragmatic model for selective laser melting with evaporation, Acta Mater. 57 (2009) 6006–6012, https://doi.org/10.1016/j.actamat.2009.08.027.
[34] J. Ning, S.Y. Liang, Analytical modeling of three-dimensional temperature distribution of selective laser melting of Ti-6Al-4V, Preprints (2018) 2018090101, https://doi.org/10.20944/preprints201809.0101.v1.
[35] I.A. Roberts, Investigation of Residual Stresses in the Laser Melting of Metal Powders in Additive Layer Manufacturing, PhD, University of Wolverhampton, Wolverhampton, United Kingdom, 2012.
[36] I. Yadroitsev, I. Yadroitseva, Evaluation of residual stress in stainless steel 316L and Ti6Al4V samples produced by selective laser melting, Virtual Phys. Prototyp. 10 (2) (2015) 67–79, https://doi.org/10.1080/17452759.2015.1026045.
[37] L. Parry, I.A. Ashcroft, R.D. Wildman, 2016. Understanding the effect of laser scan strategy on residual stress in selective laser melting through thermo-mechanical simulation, Addit. Manuf. 12 (2016) 1–15, https://doi.org/10.1016/j.addma.2016.05.014.
[38] X. Zhao, A. Iyer, P. Promoppatum, S.-C. Yao, Numerical modeling of the thermal behavior and residual stress in the direct metal laser sintering process of titanium alloy products, Addit. Manuf. 14 (2017) 126–136, https://doi.org/10.1016/j.addma.2016.10.005.
[39] J. Song, W. Wu, L. Zhang, B. He, L. Lu, X. Ni, Q. Long, G. Zhu, Role of scanning strategy on residual stress distribution in Ti-6Al-4V alloy prepared by selective laser melting, Int. J.Light.Electron. Opt 170 (2018) 342–352, https://doi.org/10.1016/j.ijleo.2018.05.128.
[40] P. Tan, F. Shen, B. Li, K. Zhou, A thermo-metallurgical-mechanical model for selective laser melting of Ti6Al4V, Mater. Des. 165 (2019) 107642, https://doi.org/10.1016/j.matdes.2019.107642.
[41] H. Li, M. Ramezani, Z. Chen, S. Singamneni, Effects of process parameters on temperature and stress distributions during selective laser melting of Ti-6Al-4V, Trans. Indian Inst. Met. 72 (2019) 3201–3214, https://doi.org/10.1007/s12666-019-01785-y.
[42] Z. Xiao, C. Chen, H. Zhu, Z. Hu, B. Nagarajan, L. Guo, X. Zeng, Study of residual stress in selective laser melting of Ti-6Al-4V, Mater. Des. 193 (2020) 108846, https://doi.org/10.1016/j.matdes.2020.108846.
[43] R.K. Ganeriwala, M. Strantza, W.E. King, B. Clausen, T.Q. Phan, L.E. Levine, D. W. Brown, N.E. Hodge, Evaluation of a thermomechanical model for prediction of residual stress during laser powder bed fusion of Ti-6Al-4V, Addit. Manuf. 27 (2019) 489–502, https://doi.org/10.1016/j.addma.2019.03.034.
[44] W. Huang, Y. Zhang, Finite element simulation of thermal behavior in single-track multiple-layers thin wall without-support during selective laser melting, J. Manuf. Process. 42 (2019) 139–148, https://doi.org/10.1016/j.jmapro.2019.04.019.
[45] A. Olleak, Z. Xi, Part-scale finite element modeling of the selective laser melting process with layer-wise adaptive remeshing for thermal history and porosity prediction, J. Manuf. Sci. Eng. 142 (12) (2020) 121006, https://doi.org/10.1115/1.4047733.
[46] P. Rangaswamy, H. Choo, M.B. Prime, M.A. Bourke, J.M. Larsen, High temperature stress assessment in SCS-6/Ti-6Al-4V composite using neutron diffraction and finite element modeling, in: THERMEC 2000 International Conference, 04.-08.12, Las Vegas, USA, 2000.
[47] C. Li, Y. Guo, X. Fang, F. Fang, A scalable predictive model and validation for residual stress and distortion in selective laser melting, CIRP Annals 67 (1) (2018) 249–252, https://doi.org/10.1016/j.cirp.2018.04.105.
[48] B. Ahmad, S.O. van der Veen, M.E. Fitzpatrick, H. Guo, Residual stress evaluation in selective-laser-melting additively manufactured titanium (Ti-6Al-4V) and inconel 718 using the contour method and numerical simulation, Addit. Manuf. 22 (2018) 571–582, https://doi.org/10.1016/j.addma.2018.06.002.
[49] C. Chen, H. Zhu, Z. Xiao, S. Liu, L. Yin, X. Zeng, The residual stress distribution of Ti-6Al-4V thin wall in the selective laser melting, Mater. Sci. Eng. 538 (2019), 012020, https://doi.org/10.1088/1757-899X/538/1/012020.
[50] S. Cao, B. Zhang, Y. Yang, Q. Jia, L. Li, S. Xin, X. Wu, Q. Hu, C.V.S. Lim, On the role of cooling rate and temperature in forming twinned α' martensite in Ti–6Al–4V, J. Alloys Compd. 813 (2020) 152247, https://doi.org/10.1016/j.jallcom.2019.152247.
[51] P. Barriobero-Vila, J. Gussone, J. Haubrich, S. Sandlöbes, J.C. Da Silva, P. Cloetens, N. Schell, G. Requena, Inducing stable α + β microstructures during selective laser melting of Ti-6Al-4V using intensified intrinsic heat treatments, Materials 10 (3) (2017) 268, https://doi.org/10.3390/ma10030268.
[52] A. Schmon, K. Aziz, G. Pottlacher, Density of liquid Ti-6Al-4V, EPJ Web Conf. 151 (2017), 04003, https://doi.org/10.1051/epjconf/20171510.
[53] C.D. Boley, S.C. Mitchell, A.M. Rubenchik, S.S.Q. Wu, Metal powder absorptivity: modeling and experiment, Appl. Opt. 55 (23) (2016) 6496–6500, https://doi.org/10.1364/AO.55.006496.

[54] A. Rubenchik, S. Wu, S. Mitchell, I. Golosker, M. LeBlanc, N. Peterson, Direct measurements of temperature-dependent laser absorptivity of metal powders, Appl. Opt. 54 (24) (2015) 7230–7233, https://doi.org/10.1364/AO.54.007230.

[55] A.M. Rubenchik, S.S.Q. Wu, V.K. Kanz, M.M. LeBlanc, W.H. Lowdermilk, M. D. Rotter, J.E. Stanley, Temperature-dependent 780-nm laser absorption by engineering grade aluminum, titanium, and steel alloy surfaces, Opt. Eng. 53 (12) (2014) 122506, https://doi.org/10.1117/1.OE.53.12.122506.

[56] M. Munsch, Reduzierung von Eigenspannungen und Verzug in der laseradditiven Fertigung, Cullivier Verlag, Göttingen, Germany, 2013.

[57] J. Yang, S. Sun, M. Brandt, W. Yan, Experimental investigation and 3D finite element prediction of the heat affected zone during laser assisted machining of Ti-6Al-4V alloy, J. Mater. Process. Technol. 210 (2010) 2215–2222, https://doi.org/10.1016/j.jmatprotec.2010.08.007.

[58] J.J.-Z. Li, STUDY OF LIQUID METALS BY ELECTROSTATIC LEVITATION, PhD, California Institute of Technology, Pasadena, USA, 2009.

[59] S. Neelakatan, P.E.J. Rivera-Díaz-del-Castillo, S. van der Zwaag, Prediction of the martensite start temperature for β titanium alloys as a function of composition, Scripta Mater. 60 (8) (2009) 611–614, https://doi.org/10.1016/j.scriptamat.2008.12.034.

[60] M. Boivineau, C. Cagran, D. Doytier, V. Eyraud, M.-H. Nadal, B. Wilthan, G. Pottlacher, Thermophysical properties of solid and liquid Ti-6Al-4V(TA6V) alloy, Int. J. Thermophys. 27 (2) (2006) 507–529, https://doi.org/10.1007/s10765-005-0001-6.

[61] M. Keller, A. Chaudhary, S. Kelly, S. Medieros, Absorption coefficient characterization in Ti-6Al-4V laser additive manufacturing, Proceedings of ICALEO (2006) 1204, https://doi.org/10.2351/1.5060759.

[62] D. Basak, R.A. Overfelt, D. Wang, Measurement of specific heat capacity and electrical resistivity of industrial alloys using pulse heating techniques, Int. J. Thermophys. 24 (6) (2003) 1721–1733, https://doi.org/10.1023/B:IJOT.0000004101.88449.86.

[63] E. Kaschnitz, P. Reiter, J.L. McClure, Thermophysical properties of solid and liquid 90Ti-6Al-4V in the temperature range from 1400 to 2300 K measured by millisecond and microsecond pulse-heating techniques, Int. J. Thermophys. 23 (1) (2002) 267–275, https://doi.org/10.1023/A:1019874916888.

[64] K.C. Mills, Recommended Values of Thermophysical Properties for Selected Commercial Alloys, Woodhead Publishing, Cambridge, UK, 2002.

[65] T. Ahmed, H.J. Rack, Phase transformations during cooling in a + b titanium alloys, Mater. Sci. Eng., A 243 (1-2) (1998) 206–211, https://doi.org/10.1016/S0921-5093(97)00802-2.

[66] E.A. Brandes, G.B. Brook, Smithells Light Metals Handbook, Butterworth-Heinemann, Oxford, UK, 1988.

[67] G. Welsch, R. Boyer, E.W. Collings, Material Properties Handbook: Titanium Alloys, ASM International, 1993.

[68] J.L. McClure, A. Cezairliyan, Measurement of the heat of fusion of titanium and a titanium alloy (90Ti-6Al-4V) by a microsecond-resolution transient technique, Int. J. Thermophys. 13 (1) (1992) 75–81.

[69] D. Benjamin, C.W. Kirkpatrick, Metals Handbook Vol. 3 - Properties and Selection: Stainless Steels, Tool Material and Special-Purpose Metals, ASM International, 1980.

[70] A. Cezairliyan, J.L. McClure, R. Taylor, Thermophysical measurements on 90Ti-6al-4V alloy above 1450 K using a transient (subsecond) technique, J. Res. Natl. Bureau .Stand.Sect. A: Physics and Chemistry 81A (2/3) (1977) 251–256, https://doi.org/10.6028/jres.081A.014.

[71] Y.S. Touloukian, R.W. Powell, C.Y. Ho, P.G. Klemens, Thermophysical Properties of Matter Vol 1. Thermal Conductivity – Metallic Elements and Alloys, Springer-Verlag, Heidelberg, Germany, 1970.

[72] W.T. Ziegler, J.C. Mullins, S.C.P. Hwa, Specific heat and thermal conductivity OF four commercial titanium alloys from 20° to 300°K, in: K.D. Timmerhaus (Ed.), Advances in Cryogenic Engineering, vol. 8, Springer Science+Business Media, LLC, 1963, pp. 268–277, https://doi.org/10.1007/978-1-4757-0528-7.

[73] J. Yang, H. Yu, J. Yin, M. Gao, Z. Wang, X. Zeng, Formation and control of martensite in Ti-6Al-4V alloy produced by selective laser melting, Mater. Des. 108 (2016) 308–318, https://doi.org/10.1016/j.matdes.2016.06.117.

[74] D.V. Gadeev, A.G. Illarionov, Determination of beta-transus temperature of two-phase titanium alloys using differential scanning Calorimetry, Solid State Phenom. 284 (2018) 259–264. https://doi.org/10.4028/www.scientific.net/SSP.284.259.

[75] B. De La Batut, O. Fergani, V. Brotan, M. Bambach, M. El Mansouri, Analytical and numerical temperature prediction in direct metal deposition of Ti-6Al-4V, J. Manuf.Mater. Process 1 (2017) 3, https://doi.org/10.3390/jmmp1010003.

[76] J.C. Heigel, P. Michaleris, E.W. Reutzel, Thermo-mechanical model development and validation of directed energy deposition additive manufacturing of Ti-6Al-4V, Addit. Manuf. 5 (2015) 9–19, https://doi.org/10.1016/j.addma.2014.10.003.

[77] P. Michaleris, Modeling metal deposition in heat transfer analyses of additive manufacturing processes, Finite Elem. Anal. Des. 86 (2014) 51–60, https://doi.org/10.1016/j.finel.2014.04.003.

[78] A. Raghavan, H.L. Wei, T.A. Palmer, T. DebRoy, Heat transfer and fluid flow in additive manufacturing, J. Laser Appl. 25 (2013), 052006, https://doi.org/10.2351/1.4817788.

[79] A. Anca, V.D. Fachinotti, G. Escobar-Palafox, A. Cardona, Computational modelling of shaped metal deposition, Int. J. Numer. Methods Eng. 85 (2011) 84–106, https://doi.org/10.1002/nme.2959.

[80] G. Vastola, G. Zhang, Q.X. Pei, Y.-W. Zhang, Controlling of residual stress in additive manufacturing of Ti-6Al-4V by finite element modeling, Addit. Manuf. 21 (2016) 231–239, https://doi.org/10.1016/j.addma.2016.05.010.

[81] B. Cheng, S. Price, J. Lydon, K. Cooper, K. Chou, On process temperature in powder-bed electron beam additive manufacturing: model development and validation, J. Manuf. Sci. Eng. 136 (2014), 061018, https://doi.org/10.1115/1.4028484.

[82] M. Jamshidinia, F. Kong, R. Kovacevic, Numerical modeling of heat distribution in the electron beam melting of Ti-6Al-4V, J. Manuf. Sci. Eng. 135 (2013), 061010, https://doi.org/10.1115/1.4025746.

[83] J. Ahn, E. He, L. Chen, R.C. Wimpory, J.P. Dear, M.C. Davies, Prediction and measurement of residual stresses and distortions in fibre laser welded Ti-6Al-4V considering phase transformation, Mater. Des. 115 (2016) 441–457, https://doi.org/10.1016/j.matdes.2016.11.078.

[84] R. Rai, Modeling of Heat Transfer and Fluid Flow in Keyhole Mode Welding, Pennsylvania State University, University Park, USA, 2008. PhD.

[85] C.C. Murgau, Microstructure Model for Ti-6Al-4V Used in Simulation of Additive Manufacturing, Lulea University of Technology, Lulea, Sweden, 2016. PhD.

[86] F. Dietzel, W. Wagner, Technische Wärmelehre, tenth ed., Vogel Buchverlag, Würzburg, Germany, 2013.

[87] R.M. Wood, The lattice constants of high purity alpha titanium, Proc. Phys. Soc. 80 (3) (1962) 783, https://doi.org/10.1088/0370-1328/80/3/323.

[88] B.W. Levinger, Lattice parameter of beta titanium at room temperature, JOM 5 (1953) 195, https://doi.org/10.1007/BF03397474.

[89] Y. Zhang, J.R.G. Evans, S. Yang, Corrected values for boiling points and enthalpies of vaporization of elements in handbooks, J. Chem. Eng. Data 56 (2011) 328–337, https://doi.org/10.1021/je1011086.

[90] S.D. Proell, W.A. Wall, C. Meier, On phase change and latent heat models in metal additive manufacturing process simulation, Adv.Model. Simulat.Eng. Sci. 7 (24) (2020) 1–32, https://doi.org/10.1186/s40323-020-00158-1.

[91] H. Gu, H. Gong, J.J.S. Dilip, D. Pal, A. Hicks, H. Doak, B. Stucker, Effects of powder variation on the microstructure and tensile strength of Ti-6Al-4V parts fabricated by selective laser melting, in: Proceedings of the 25th Annual International Solid Freeform Fabrication Symposium, 2014, pp. 470–483. Texas, USA.

[92] A.V. Gusarov, E.P. Kovalev, Model of thermal conductivity on powder beds, Phys. Rev. B 80 (2009), 024202, https://doi.org/10.1103/PhysRevB.80.024202.

[93] M. De Beer, P.G. Rousseau, C.G. Du Toit, A review of methods to predict the effective thermal conductivity of packed pebble beds, with emphasis on the near-wall region, Nucl. Eng. Des. 331 (2018) 248–262, https://doi.org/10.1016/j.nucengdes.2018.02.029.

[94] L.C. Wei, L.E. Ehrlich, M.J. Powell-Palm, C. Montgomery, J. Beuth, J.A. Malen, Thermal conductivity of metal powders for powder bed additive manufacturing, Addit. Manuf. 21 (2018) 201–208, https://doi.org/10.1016/j.addma.2018.02.002.

[95] A.M. Beese, B.E. Carroll, Review of mechanical properties of Ti-6Al-4V made by laser-based additive manufacturing using powder feedstock, JOM 68 (3) (2016) 724–734, https://doi.org/10.1007/s11837-015-1759-z.

[96] J. Tong, C.R. Bowen, J. Persson, A. Plummer, Mechanical properties of titanium-based Ti–6Al–4V alloys manufactured by powder bed additive manufacture, Materials Science and Technoloy 33 (2) (2017) 138–148, https://doi.org/10.1080/02670836.2016.1172787.

[97] A. Mertens, S. Reginster, H. Paydas, Q. Contrepois, T. Dormal, O. Lemaire, J. Lecomte-Beckers, Mechanical properties of alloy Ti–6Al–4V and of stainless steel 316L processed by selective laser melting: influence of out-of-equilibrium microstructures, Powder Metall. 57 (3) (2014) 184–189, https://doi.org/10.1179/1743290114Y.0000000092.

[98] M. Simonelli, Y.Y. Tse, C. Tuck, Effect of the build orientation on the mechanical properties and fracture modes of SLM Ti–6Al–4V, Mater. Sci. Eng., A 616 (2014) 1–11, https://doi.org/10.1016/j.msea.2014.07.086.

[99] C. Qiu, N.J.E. Adkins, M.M. Attallah, Microstructure and tensile properties of selectively laser-melted and of HIPed laser-melted Ti-6Al-4V, Mater. Sci. Eng., A 578 (2013) 230–239, https://doi.org/10.1016/j.msea.2013.04.099.

[100] J.J. Lewandowski, M. Seifi, Metal additive manufacturing: a review of mechanical properties, Annu. Rev. Mater. Res. 46 (1) (2016) 151–186, https://doi.org/10.1146/annurev-matsci-070115-032024.

[101] L. Thijs, F. Verhaeghe, T. Craeghs, J. Van Humbeeck, J.-P. Kruth, A study of microstructural evolution during selective laser melting of Ti-6Al-4V, Acta Mater. 58 (2010) 3303–3312, https://doi.org/10.1016/j.actamat.2010.02.004.

[102] P. Edwards, M. Ramulu, Fatigue performance evaluation of selective laser melted Ti–6Al–4V, Mater. Sci. Eng., A 598 (2014) 327–337, https://doi.org/10.1016/j.msea.2014.01.041.

[103] D. Agius, K. Kourousis, C. Wallbrink, A review of the as-built SLM Ti-6Al-4V mechanical properties towards achieving fatigue resistant designs, Metals 8 (1) (2018) 75, https://doi.org/10.3390/met8010075.

[104] G. Kasperovich, J. Hausmann, Improvement of fatigue resistance and ductility of TiAl6V4 processed by selective laser melting, J. Mater. Process. Technol. 220 (2015) 202–214, https://doi.org/10.1016/j.jmatprotec.2015.01.025.

[105] F. Cao, T. Zhang, M.A. Ryder, D.A. Lados, A review of the fatigue properties of additively manufactured Ti-6Al-4V, JOM 70 (2018) 349–357, https://doi.org/10.1007/s11837-017-2728-5.

[106] Q. Yan, B. Chen, N. Kang, X. Lin, S. Lu, K. Kondoh, S. Li, J.S. Li, Comparison study on microstructure and mechanical properties of Ti-6Al-4V alloys fabricated by powder-based selective-laser-melting and sintering methods, Mater. Char. 164 (2020) 110358, https://doi.org/10.1016/j.matchar.2020.110358.

[107] N. Dumontet, D. Connétable, B. Malard, B. Viguier, Elastic properties of the α' martensitic phase in the Ti-6Al-4V alloy obtained by additive manufacturing, Scripta Mater. 167 (2019) 115–119, https://doi.org/10.1016/j.scriptamat.2019.03.042.

[108] J. He, D. Li, W. Jiang, L. Ke, G. Qin, Y. Ye, Q. Qin, D. Qiu, The martensitic transformation and mechanical properties of Ti-6Al-4V prepared via selective laser melting, Materials 12 (2) (2019) 321, https://doi.org/10.3390/ma12020321.
[109] W. Ming, J. Chen, Q. An, M. Chen, Dynamic mechanical properties and machinability characteristics of selective laser melted and forged Ti-6Al-4V, J. Mater. Process. Technol. 271 (2019) 284–292, https://doi.org/10.1016/j.jmatprotec.2019.04.015.
[110] E. Santecchia, P. Mengucci, A. Gatto, E. Bassoli, L. Denti, B. Rutkowski, A. Czyrska-Filemonowicz, G. Barucca, Powder bed fusion of biomedical Co-Cr-Mo and Ti-6Al-4V alloys: microstructure and mechanical properties, Adv. Mater. Res. 1151 (2019) 3–7. https://doi.org/10.4028/www.scientific.net/AMR.1151.3.
[111] P. Tao, J. Zhong, H. Li, S. Gong, Q. Xu, Microstructure, mechanical properties, and constitutive models for Ti–6Al–4V alloy fabricated by selective laser melting (SLM), Metals 9 (4) (2019) 447, https://doi.org/10.3390/met9040447.
[112] L. Zhou, T. Yuan, J. Tang, J. He, R. Li, Mechanical and corrosion behavior of titanium alloys additively manufactured by selective laser melting – a comparison between nearly β titanium, α titanium and α + β titanium, Opt Laser. Technol. 119 (2019) 105625, https://doi.org/10.1016/j.optlastec.2019.105625.
[113] P. Hartunian, M. Eshraghi, Effect of build orientation on the microstructure and mechanical properties of selective laser-melted Ti-6Al-4V alloy, J. Manuf.Mater. Process 2 (4) (2018) 69, https://doi.org/10.3390/jmmp2040069.
[114] J. Stef, A. Poulon-Quintin, A. Redjaimia, J. Ghanbaja, O. Ferry, M. de Sousa, M. Gouné, Mechanism of porosity formation and influence on mechanical properties in selective laser melting of Ti-6Al-4V parts, Mater. Des. 156 (2018) 480–493, https://doi.org/10.1016/j.matdes.2018.06.049.
[115] A. Zafari, M.R. Barati, K. Xia, Controlling martensitic decomposition during selective laser melting to achieve best ductility in high strength Ti-6Al-4V, Mater. Sci. Eng., A 744 (2019) 445–455, https://doi.org/10.1016/j.msea.2018.12.047.
[116] H. Ali, L. Ma, H. Ghadbeigi, K. Mumtaz, In-situ residual stress reduction, martensitic decomposition and mechanical properties enhancement through high temperature powder bed pre-heating of Selective Laser Melted Ti-6Al-4V, Mater. Sci. Eng., A 695 (2017) 211–220, https://doi.org/10.1016/j.msea.2017.04.033.
[117] D.J. Agius, Cyclic Plasticity of Aerospace Metals: I. Modelling of Aluminium 7075-T6 for Structural Fatigue Analysis, II. Experimental Characterisation and Modelling of Additively Manufactured Ti-6Al-4V, PhD, RMIT University, Melbourne, Australia, 2017.
[118] T.M. Mower, M.J. Long, Mechanical behavior of additive manufactured, powder-bed laser-fused materials, Mater. Sci. Eng., A 651 (2016) 198–213, https://doi.org/10.1016/j.msea.2015.10.068.
[119] G.M. Ter Haar, T. Becker, D.C. Blaine, Influence OF heat treatments ON the microstructure and tensile behaviour OF selective laser melting-produced TI-6AL-4V parts, S. Afr. J. Ind. Eng. 27 (3) (2016) 174–183, https://doi.org/10.7166/27-3-1663.
[120] V. Cain, L. Thijs, J. van Humbeeck, B. van Hooreweder, R. Knutsen, Crack propagation and fracture toughness of Ti-6Al-4V alloy produced by selective laser melting, Addit. Manuf. 5 (2015) 68–76, https://doi.org/10.1016/j.addma.2014.12.006.
[121] H. Gong, K. Rafi, H. Gu, G.D. Janaki Ram, T. Starr, B. Stucker, Influence of defects on mechanical properties of Ti–6Al–4V components produced by selective laser melting and electron beam melting, Mater. Des. 86 (2015) 545–554, https://doi.org/10.1016/j.matdes.2015.07.147.
[122] K.D. Rekedal, D. Liu, Fatigue life of selective laser melted and hot isostatically pressed Ti-6Al-4V absent of surface machining, in: Proceedings of 56th AIAA/ASCE/AHS/ASC Structures, Structural Dynamics, and Materials Conference, Kimmissee, USA, 2015, p. 894.
[123] X. Zhao, S. Li, M. Zhang, Y. Liu, T.B. Sercombe, S. Wang, Y. Hao, R. Yang, L. E. Murr, Comparison of the microstructures and mechanical properties of Ti–6Al–4V fabricated by selective laser melting and electron beam melting, Mater. Des. 95 (2016) 21–31, https://doi.org/10.1016/j.matdes.2015.12.135.
[124] S. Leuders, T. Lieneke, S. Lammers, T. Tröster, T. Niendorf, On the fatigue properties of metals manufactured by selective laser melting – the role of ductility, J. Mater. Res. 29 (17) (2014) 1911–1919, https://doi.org/10.1557/jmr.2014.157.
[125] H. Gong, Generation and Detection of Defects in Metallic Parts Fabricated by Selective Laser Melting and Electron Beam Melting and Their Effects on Mechanical Properties, Electronic Theses and Dissertations, 2013, p. 515, https://doi.org/10.18297/etd/515.
[126] S. Leuders, M. Thöne, A. Riemer, T. Niendorf, T. Tröster, H.A. Richard, H.J. Maier, On the mechanical behaviour of titanium alloy TiAl6V4 manufactured by selective laser melting: fatigue resistance and crack growth performance, Int. J. Fatig. 48 (2013) 300–307, https://doi.org/10.1016/j.ijfatigue.2012.11.011.
[127] H.K. Rafi, N.V. Karthik, H. Gong, T.L. Starr, B.E. Stucker, Microstructures and mechanical properties of Ti-6Al-4V parts fabricated by selective laser melting and electron beam melting, J. Mater. Eng. Perform. 22 (12) (2013) 3872–3883, https://doi.org/10.1007/s11665-013-0658-0.
[128] M. Thöne, S. Leuders, A. Riemer, T. Tröster, H.A. Richard, Influence of heat-treatment on Selective Laser Melting products – e.g. Ti-6Al-4V, in: Proceedings of the 23rd Annual International Solid Freefrom Fabrication Symposium, 2012, pp. 492–498. Austin, USA.
[129] B. Vrancken, L. Thijs, J.-P. Kruth, J. van Humbeeck, Heat treatment of Ti-6Al-4V produced by selective laser melting: microstructure and mechanical properties, J. Alloys Compd. 541 (2012) 177–185, https://doi.org/10.1016/j.jallcom.2012.07.022.
[130] T. Vilaro, C. Colin, J.D. Bartout, As-Fabricated and heat-treated microstructures of the Ti-6Al-4V alloy processed by selective laser melting, Metall. Mater. Trans. 42 (10) (2011) 3190–3199, https://doi.org/10.1007/s11661-011-0731-y.
[131] L. Facchini, E. Magalini, P. Robotti, A. Molinari, S. Höges, K. Wissenbach, Ductility of a Ti-6Al-4V alloy produced by selective laser melting of prealloyed powders, Rapid Prototyp. J. 16 (6) (2010) 450–459, https://doi.org/10.1108/13552541011083371.
[132] B. Vandenbroucke, J.-P. Kruth, Selective laser melting of biocompatible metals for rapid manufacturing of medical parts, Rapid Prototyp. J. 13 (4) (2007) 196–203, https://doi.org/10.1108/13552540710776142.
[133] D.A. Hollander, M. von Walter, T. Wirtz, R. Sellei, B. Schmidt-Rohlfing, O. Paar, H.-J. Erli, Structural, mechanical and in vitro characterization of individually structured Ti-6Al-4V produced by direct laser forming, Biomaterials 27 (7) (2006) 955–963, https://doi.org/10.1016/j.biomaterials.2005.07.041.
[134] S. Manikandan, S. Ramanathan, V. Ramakrishnan, Thermophysical properties of titanium (Ti-6Al-4V) alloy in the temperature range of -125° C to 550° C, Int. J. ChemTech.Res. 9 (2) (2016) 10–19.
[135] Y. Chong, T. Bhattacharjee, J. Yi, S. Shibata, N. Tsuji, Mechanical properties of fully martensitic microstructure in Ti-6Al-4V alloy transformed from refined beta grains obtained by rapid heat treatment (RHT), Scripta Mater. 138 (2017) 66–70, https://doi.org/10.1016/j.scriptamat.2017.05.038.
[136] J. Sieniawski, W. Ziaja, K. Kubiak, M. Motyka, Microstructure and mechanical properties of high strength two-phase titanium alloys, in: J. Sieniawski, W. Ziaja (Eds.), Titanium Alloys – Advances in Properties Control, InTechOpen, London, UK, 2013, pp. 69–80, https://doi.org/10.5772/56197.
[137] W.-S. Lee, C.-F. Lin, Plastic deformation and fracture behaviour of Ti-6Al-4V alloy loaded with high strain rate under various temperatures, Mater. Sci. Eng. A241 (1998) 48–59.
[138] G. Lütjering, Influence of processing on microstructure and mechanical properties of (α+β) titanium alloys, Mater. Sci. Eng. A243 (1998) 32–45.
[139] Y.L. Hao, S.J. Li, B.B. Sun, M.L. Sui, R. Yang, Ductile titanium alloy with low Poisson's ratio, Phys. Rev. Lett. 98 (2007) 216405, https://doi.org/10.1103/PhysRevLett.98.216405;
[140] K. Bartsch, D. Herzog, B. Bossen, C. Emmelmann, Material Modeling of Ti-6Al-4V Alloy Processed by Laser Powder Bed Fusion for Application in Macro-Scale Process Simulation, TUHH Universitätsbibliothek, 2020. https://doi.org/10.15480/336.2887.